Hydrogen-free catalytic conversion of highly concentrated glycerol solution: Influence of Si/Al molar ratio in Cu/SBA-15 catalysts

Jorge Gajardo[a,1], Julio Colmenares-Zerpa[a,b,1], A.F. Peixoto[c], D.S.A. Silva[d], F. Gispert-Guirado[e], J. Llorca[f], E.A.Urquieta-Gonzalez[d, g], J.B.O. Santos[d], M.G. Álvarez[h,]*, R.J. Chimentão[a,]*

[a] Laboratorio de Investigación de Procesos Catalíticos y Adsorción (LIPROCAD), Departamento de Fisicoquímica, Facultad de Ciencias Químicas, Universidad de Concepción, Concepción, Casilla 160-C, Chile.

[b] Laboratorio de Cinética y Catálisis, Facultad de Ciencias, Universidad de Los Andes, Mérida 5101, Venezuela.

[c] LAQV-REQUIMTE, Departamento de Química e Bioquímica, Faculdade de Ciências da Universidade do Porto, Rua do Campo Alegre, 4169-007 Porto, Portugal.

[d] Departamento de Engenharia Química, Universidade Federal de São Carlos, São Carlos, Brasil.

[e] Servei de Recursos Científics, Universitat Rovira i Virgili, Tarragona 43007, Spain.

[f] Department of Chemical Engineering, Center for Research in Multiscale Science and Engineering, Universitat Politècnica de Catalunya, Eduard Maristany 10-14, 08019 Barcelona, Spain.

[g] Research Center on Advanced Materials and Energy, Federal University of São Carlos, C. Postal 676, CEP, 13565-905, São Carlos, SP, Brasil.

[h] GIR-QUESCAT. Departamento de Química Inorgánica, Facultad de Ciencias Químicas, Universidad de Salamanca. Spain.

[1] These authors contributed equally to this work.

* Corresponding authors: mgalvarez@usal.es; rchimenton@udec.cl

Abstract

Catalytic conversion of glycerol to C_3 products using advanced functional materials is an economical and efficient approach to promoting sustainable energy development. Selective glycerol dehydration to hydroxyacetone (HA) is one such alternative and requires an appropriate balance of catalyst texture, structure, and acidity. In this study, different Cu-based catalysts supported on SBA-15 with different Si/Al molar ratios (2, 10, 15 and ∞) were prepared using the "pH-adjusting" method and ammonia evaporation method and they were evaluated for the dehydration of glycerol at high concentration (80 wt%.) in liquid phase to hydroxyacetone under inert N_2 atmosphere. The formation of 1,2-PDO was also observed even under N_2 inert atmosphere conditions. The catalysts were characterized by ICP-MS, N_2 adsorption-desorption, XRD, HRTEM, H_2-TPR, passivation of N_2O, NH_3-TPD, TPO, FTIR, FTIR-OH, Py-FTIR and XPS. The Al chemical environment and the Si/Al molar ratio of the supports show a remarkable effect on the catalytic performance. The highest catalytic activity was obtained with the Si/Al = 15 molar ratio, reaching a conversion of around 35% at 120 min of reaction and a selectivity of 84% to hydroxyacetone at 90 min of reaction. While lower Si/Al molar ratios led to a decrease in catalytic activity and an increase in product distribution. The isomorphic incorporation of Al into the SBA-15 promotes the interlinking cooperative between the properties of textural, acidity, structural, and stability of the catalyst. HRTEM and HAADF-STEM images show a well-defined hexagonal arrangement even when the CuO phase is added to the mesoporous materials with high Al loadings. At high heteroatom loadings, the typical hexagonal arrangement of the mesostructure was preserved but a decrease in the long-range order was observed. The presence of mononuclear and oligonuclear $Cu^{\delta+}$ species, which is related to their coordination environment and their position in the mesoporous network, was dependent on the variation of the Si/Al molar ratio. The prominent catalytic performance at the Si/Al = 15 ratio can be attributed to an optimal cooperative effect of the structural defects and electronic promotion produced by the Al species, which favors the conversion of glycerol to HA. While the increase in the selectivity of 1,2-PDO observed with the molar ratio Si/Al = 2 is associated with a conjugation between the higher availability of acid sites on the surface that promote the dehydration of glycerol and the domain size of copper species which would be acting as dehydrogenating sites of glycerol, forming H_2 *in-situ* leading to the conversion of HA into 1,2-PDO.

Keywords: *glycerol dehydration, hydroxyacetone, mesoporous material, copper, high glycerol concentration, Si/Al molar ratio.*

Highlights

- Synthesis of Cu/SBA-15 with different Si/Al ratios.
- Textural, structural, acid, and surface properties change with the Si/Al ratio.
- High concentration glycerol dehydration under an inert atmosphere.
- Intra-framework Al species were formed in the Cu/Al-SBA-15 with the lower Al load.
- Incorporation of copper by ammonia-evaporation (AE) method.

1. Introduction

The need to find new energy resources due to increasing energy demand and environmental implications has led to a vision of sustainable use of resources. In this sense, research on catalytic transformations of different biomass-derived compounds is currently active. Especially, glycerol is considered one of the most important biomass-derived starting platform molecules. This has been generated over the years from the biodiesel production and it is estimated that biodiesel production will continue to grow, with projected average annual production growth of 17.5% from 2023 to 2027**[1]**. Hence, the transformation and valorization of glycerol represents an important contribution to the conversion of renewable and clean raw materials and the development of clean processes to overcome both environmental and economic considerations**[2, 3]**.

Among the various strategies for glycerol valorization, the pursuit of sustainable catalytic pathways to produce C_3 chemicals has emerged as a highly relevant possibility**[2, 4]**. The selective dehydration towards hydroxyacetone (HA) is interesting for the sustainable and atomically economic advantages it offers. HA serves as a crucial intermediate in the production of propylene glycol, propionaldehyde, acetaldehyde, furan derivatives, and other compounds derived from petroleum**[5]**. Traditionally, HA has been synthesized by several processes, catalytic**[6]** and biological**[7, 8]**. However, many of these methods involve multiple steps, rendering them economically unfeasible when considering factors such as low yield values, the extensive use of expensive reactants, and the cost of effluent disposal**[9]**. Producing HA from glycerol sourced from biomass could potentially reduce production costs by up to 10 times compared to petroleum-based production**[10]**. Therefore, with its advantage in the carbon-atom economy, this type of production offers grated economic viability and benefits compared to conventional methods reliant on petroleum substances.

A wide variety of heterogeneous catalysts have been used in the conversion of glycerol to HA, with transition metal-based catalysts being potential candidates for this application**[9]**. Inexpensive transition metal catalysts such as Ni, Co, and Cu remain more competitive than noble metals**[4, 11]**. Copper-based catalysts are distinguished by their low cost, reduced toxicity compared to nickel or cobalt, and superior resistance to poisoning compared to noble metals. Cu possesses a low ability to produce C–C bond cleavage rendering it a convenient and environmentally friendly option for the dehydration of glycerol to HA**[12, 13]**. Indeed, Cu-based catalysts demonstrate higher viability in achieving elevated glycerol conversion and selectivity towards HA. Sato et al.**[14]** in their study of the gas-phase reaction of glycerol over copper-based catalysts (Al_2O_3, Cr_2O_3 supported Cu catalysts), found that both supported copper as well as pure copper metal were effective catalysts for the dehydration of glycerol to produce HA under inert conditions.

Additionally, according to the liquid phase glycerol dehydration mechanism elucidated by Mane et al.**[15]**, glycerol dehydration is not only catalyzed by the acid sites but also by the Cu metal sites present in the catalyst. Similar findings were reported by the group of Gabrysch et al.**[16]** when they sought to define the active site for the determining step of glycerol dehydration on Cu/ZrO_2 catalysts when studying the glycerol dehydrogenation reaction. Nevertheless, despite their catalytic efficiency, copper-based catalysts pose a significant challenge; generally, copper particles tend to sinter easily during the catalytic reaction**[17]**. Hence, one of the strategies to improve their stability is the confinement of these species on a support. The support plays a crucial role in catalyst composition, influencing the interaction with the active phases, which in turn affects the stability and activity of the catalyst**[18, 19]**. In this regard, several studies report the improvement of the Cu activity by dispersing it on acid supports such as SiO_2**[20, 21]**, ZrO_2**[22]**, SBA-15**[23]**, Al_2O_3**[24]**, Hydrotalcites-type materials (HTs)**[13]** and ZSM-5**[25]**. Some researchers stated that silicon-based supports could facilitate the generation of well-dispersed Cu species and are preferable to other acidic supports for achieving better HA yields**[26]**. The preparation method, on the other hand, plays a crucial role in the optimization of copper species. Several preparation methods have been explored to achieve improved dispersion of copper particles in silica, most commonly impregnation, ammonia evaporation (AE) hydrothermal method, ion exchange, precipitation-gel, sol-gel methods, and others**[9, 27]**. Of these, the ammonia evaporation method can effectively disperse the copper and provide a high copper loading on the support**[28, 29]**. This has been attributed to the fact that the formation of phyllosilicates by this method results in a strong interaction between copper and silica. Although, the ammonia evaporation method has attracted considerable attention in the preparation of Cu/SiO_2, but lately, the recent trend has focused on the application of mesostructured siliceous materials due to their potential features**[30, 31]**.

SBA-15 mesoporous silica has been widely regarded as a promising catalytic support. This type of silica exhibits remarkable characteristics such as a well-defined porous architecture with a hexagonal mesostructure, large surface area, and comparatively thicker walls that confer good hydrothermal stability. These features enable it the ability to incorporate metal atoms within the mesopores, making it a suitable platform for the dispersion of copper species**[32-34]**. In addition, this uniform mesopore system not only provides a wide space for the incorporation of active sites but also combines the advantages of high accessibility to them and efficient mass transport effects**[34, 35]**. However, despite its qualities of structural uniformity, size, order, and uniform distribution of its pores, all of which are often not sufficient to satisfy certain application requirements, particularly due to their inert character because of their overall neutral framework and the absence of active components.

The literature reports that the dehydration of glycerol requires catalysts with appropriate acidity and a well-balanced combination of material structure and porosity. Numerous studies suggest that Lewis acid centers enhance selectivity towards HA**[10, 13, 15, 36]**. HA formation from glycerol involves a complex reaction pathway including direct dehydration of primary and/or secondary–hydroxyl group or dehydrogenation followed by dehydration, depending on the type and strength of acid sites present on the catalyst surface. Extensive research has been conducted on the glycerol dehydration reaction in the gas-phase mode**[37-39]**, with the majority of studies involving the utilization of hydrogen in the formation of 1,2-propanediol (1,2-PDO)**[11, 40]** but only a few articles focused on the liquid phase can be found in the literature**[15, 22, 41]**. Most of the vapor phase studies have been performed at high temperatures, leading to reduced selectivity towards HA due to the formation of acrolein and other by-products. In addition, these processes can result in rapid catalyst deactivation due to the extensive formation of carbonaceous deposits on the surface**[42]**. Thus, liquid-phase glycerol dehydration may be preferable for achieving high selectivity towards HA.

Considering that Lewis acidic sites are required to promote glycerol dehydration to the formation of HA, introducing a heteroatom into the structure of SBA-15 is an effective approach to enhance the catalytic role of this material**[43]**. Hence, the functionalization of SBA-15 by introducing heteroatoms in its structure becomes much more indispensable to exceed certain limitations. Its functionalization capacity allows optimizing this system by insertion of metal ions or heteroatoms into the neutral silica framework thereby creating materials with diverse acid-base or redox properties suitable for various scientific and technological applications**[32, 33]**. Different heteroatoms have been incorporated such as Al**[44-46]**, Ga**[47]**, Fe**[48]**, Zr**[49]**, Ti**[50]**, or Nb**[51]**, with the aim of tuning and improving either the acid-base or redox properties of SBA-15. It is widely reported that by changing the Al loading on SBA-15 silica it is possible to design the surface acid site density. Incorporating Al into the siliceous mesoporous network is effective for the creation of acid sites making it suitable for use as an acidic solid catalyst or as a carrier material for the dispersion of metal nanoparticles (NPs) and also to improve their hydrothermal stability**[46, 52]**. The coordination environment of the aluminum species influences the nature and strength of the acid sites that these species can provide to SBA-15, showing a linear relationship between the ratio of Brönsted/Lewis acid sites (C_B/C_L) and the proportion of tetrahedral species**[45]**. Aluminum is considered the most appropriate element to be inserted into the silicon framework of the SBA-15 due to its similar properties and atomic size referred to the silicon element. In addition, it has proven to be a valuable alternative for the generation of surface acid sites due to its small size and high charge density**[53]**.

Nevertheless, the incorporation of aluminum into the mesoporous silica is not straightforward and requires fine control of the synthesis procedures**[46, 54]**. Normally the synthesis of SBA-15 is carried out in an acidic medium (pH ~ 1) in order to precipitate silica (isoelectric point, IEP ~ 2), increase the cationic charge density of the medium, and thus promote cooperative self-assembly of the silicon ions with the pre-formed template structure. This assembly is achieved through hydrolysis and condensation reactions, resulting in the formation of a hybrid organic-inorganic interface and consequently the formation of the hexagonal mesophase of SBA-15**[33]**. The pH level significantly affects the solubility of the aluminum precursor. At a pH ~ 1, aluminum exists primarily in its cationic form (Al^{3+}), which hinders its condensation onto silicon species to form Si–O–Al bonds due to electrostatic repulsion between the Al^{3+} ions and silica species**[55, 56]**. Additionally, in acidic hydrothermal conditions, the dissociation of Al–O–Si bonds is promoted, and the difference in hydrolysis rates between silica and aluminum is typically substantial, resulting in less efficient insertion of Al into the mesostructure.

Several synthetic strategies to introduce the Al species in the SBA-15 have been adopted to overcome these circumstances, including direct synthesis**[57, 58]**, post-synthesis**[59]**, and "pH-adjusting"**[55, 56, 60]**. The pH-adjusting method has been proven to be the most efficient method to achieve high levels of aluminum incorporation**[55, 60-62]**. The two-step pH-adjusting method has been developed to enhance the insertion of heteroatoms such as Al into the walls of ordered mesoporous silica materials under these strongly acidic conditions. In this method, the heteroatom source is added to the initial reaction mixture in a strongly acidic medium (pH ~ 0). Once the hexagonal mesophase is formed, the pH value of the system is adjusted to a neutral pH of 7.5, followed by a hydrothermal treatment for an additional period of time, during which a large number of heteroatoms can be isomorphically introduced into the mesophase**[55, 60]**. Through, the "pH-adjustment" step, random incorporation of Al into the structure of SBA-15 is minimized and considerable differences between the Si/Al ratios of the initial gel and the final product are avoided. It should be noted that aspects such as the synthesis approach as well as the selection of the variables of reaction involved such as the nature of the Si**[63]** and Al**[64]** precursors used, the type of acids used as media**[43, 65, 66]**, the control of the H_2O/HCl molar ratio**[44, 57]**, the temperature and time of the synthesis of initial gel mixture**[66, 67]**, the order in which the Si and Al precursors are added in the hydrothermal synthesis (simultaneously, separately, or in intervals)**[68],** among others**[53, 57, 62],** can influence the physicochemical properties and the quality of the final material.

Considering this background outlined regarding the adjustment of the synthesis parameters, the incorporation of high aluminum loading in the SBA-15 structure was studied. Different Si/Al molar ratios

were evaluated (15, 10, 2, and ∞). The Al-SBA-15 materials in this study were synthesized by the "pH-adjusting" method reported by Wu et al.**[60]** with modifications such as the aluminum source, shorter time reaction of gel formation, and a temperature of 60 °C in the preparation of the initial gel mixture. The role of high aluminum loading incorporation in the texture, structure, acidity, and surface properties of SBA-15 was assessed. In addition, a series of Cu-based catalysts supported on the SBA-15 with different Si/Al molar ratios (2, 10, 15, and ∞) were prepared and evaluated in the liquid phase dehydration of glycerol under an inert atmosphere of nitrogen. Copper species were introduced on Al-SBA-15 materials by the ammonia evaporation (AE) method. The change in the aluminum loading in the structure of SBA-15 affected the structural, textural, and acidity properties of the catalysts and the interaction of Cu species with Al-SBA-15 support. These catalyst descriptors were correlated with the dehydration of glycerol.

2. Experimental

2.1. Support synthesis

The SBA-15 samples containing aluminum were synthesized by the "pH-adjusting" method modified from the literature**[60]**. The methodology adopted for the synthesis of these materials is detailed in the supplementary material and illustrated in Scheme S1.

2.2. Catalysts synthesis

All nominal loadings were 5 wt%. metallic Cu. The copper catalysts were prepared by the AE method**[69]** and the methodology adopted for the synthesis of these materials is detailed in Scheme S1 of the supplementary material. The appropriate amount of $Cu(NO_3)_2 \cdot 3H_2O$ (Merck, 99%) was dissolved in a certain volume of deionized water (to maintain the same concentration in the final solid; at a ratio of 0.2386 g of the precursor salt to 1.0 mL of distilled water). An approximate volume of 14 mL of 28 wt% of ammonia aqueous solution was added and the solution was stirred at 25 °C for 10 min to form the ammonia copper complex solution. Then the amount of support was dispersed in the ammonia copper complex solution. The slurry was stirred for 20 min at 25 °C and subsequently, the temperature was raised to 90 °C to evaporate ammonia. After this process, the solid was dried for 2 h at 90 °C and underwent a calcination treatment from room temperature to 400 °C (2 $°C \cdot min^{-1}$) for 4 h.

2.3 Characterization

2.3.1. Chemical composition

Copper loading of the catalysts was determined by inductively coupled plasma spectrometer (ICP-MS) on Thermo Fisher Scientific iCAP RQ ICP-MS equipment. Samples were digested, previously to the analysis, in a mixture of acids HF: HCl (3:7) in a Milestone microwave apparatus at 120 °C for 15 min.

The local variation in the composition of the samples and the Si/Al molar ratio of the resulting samples were determined by Energy Dispersive X-ray Spectroscopy (EDS) analyses on a VEGA3 EASYPROBE SBU (TESCAN) unit coupled to an OXFORD energy dispersive X-ray (EDS) spectrometer using a voltage of 20 kV and a working distance of 12 mm. The EDS technique is used for semiquantitative elemental analysis of the sample, by spectral method and mapping.

An X-ray fluorescence spectrometer (Shimadzu EDX-720 energy dispersive spectrometer) was used to identify the Si/Al molar ratio of the prepared samples. The equipment has an X-ray tube with a rhodium (Rh) anode that operates between 5-50 kV and 1-1000 μA. This technique allows qualitative and quantitative analysis of elements with atomic weights between sodium (Na) and uranium (U).

2.3.2. Textural and structural properties

N_2 adsorption-desorption analyses at -196 °C were performed in a Tristar II series Micromeritics to evaluate the textural properties of the samples. The samples (approximately, 100 mg) were dried in an oven overnight and then degassed under an N_2 flow at 120 °C for 2 h, prior to measurements. Multi-point BET (S_{BET}) surface area value was estimated from P/P_0 values within the range of 0.05-0.30. The total pore volume (V_P) was determined from adsorption data at a P/P_0 value of 0.95 and the pore size distribution of the samples was determined by the adsorption isotherm of the BJH method.

X-ray diffraction measurements (XRD) were made using a Bruker-AXS D8-Advance diffractometer with vertical theta-theta goniometer, incident- and diffracted-beam Soller slits of 2.5º, a fixed 0.5º receiving slit and an automatic air-scattering knife on the sample surface. Low-angle X-ray diffraction patterns were recorded for 2θ = 0.5-10º with an angular step of 0.02º at a step/time of 1.0 s using the software option Variable Detector Opening. Meanwhile, the wide angles X-ray diffraction was recorded for 2θ = 5-80º with an angular step of 0.02º at a step/time of 0.5 s. CuK_α radiation was obtained from a copper X-ray tube operated at 40 kV and 40 mA. Diffracted X-rays were detected with a PSD detector LynxEye-XE-T with an opening angle of 2.94º. Samples were deposited on a low-background (Si (510)) support. The diffractograms were interpreted with the software TOPAS by considering a hexagonal cell**[70]** and refining only the *a* parameter and the peak width. Profile fitting**[70]** was performed with the TOPAS v6 software**[71, 72]**. The background was modeled with a 3rd order Chebyshev polynomial. The instrumental contribution to the diffraction profile was calculated with the LaB_6 (NIST SRM 660c). The peak width of each phase was modeled with the Double-Voigt Approach**[73, 74]** by considering only the Lorentzian contribution of the crystallite size effect and discarding any contribution of the microstrain to the peak width. The average integral breadth was obtained from the resulting fitted Voigt function to the whole diffractogram. The Scherrer equation**[75]** was then applied to obtain the apparent crystallite size.

The morphology and the pore structure of the samples and distribution of Cu in the catalysts were observed by high-resolution transmission electron microscopy (HRTEM) and high-angle annular dark-field scanning transmission electron microscopy (HAADF-STEM). The micrographs were obtained on a FEI Tecnai F20

microscope equipped with a field emission source with a point-to-point resolution of 0.19 nm and an accelerating voltage of 200 kV. The sample was suspended in methanol and a drop was deposited on a copper grid coated with a carbon film.

2.3.3. Spectroscopic studies

The concentration of acidic sites (Brönsted and Lewis) of the materials was determined using *in-situ* Fourier Transform Infrared (FTIR) spectroscopy technique with adsorbed pyridine using a transmission cell with CaF_2 windows in a Bruker spectrometer (Vertex 70) equipped with an MCT detector. The background was carried out at 150 °C under an Ar atmosphere (100 mL·min^{-1}) after 30 min of heating. For analysis, a 12 mm sample self-supporting pellet was pretreated at 350 °C under an Ar atmosphere (100 mL·min^{-1}) for 60 minutes. Then, the system was cooled to 150 °C, and pyridine vapor was injected until the sample was completely saturated. Excess physisorbed pyridine was removed with Ar flow (100 mL·min^{-1}). The spectra of the samples without and with adsorbed pyridine were subtracted. The acid sites were quantified based on the Lambert-Beer equation:

$$A_i = \frac{\varepsilon_i W C_i}{S} \qquad \text{(Eq. 1)}$$

Where A_i (cm^{-1}), ε_i (cm·μmol^{-1}), W (mg), C_i (mmol·g^{-1}), and S (cm^2) are the integrated absorbance, integrated molar extinction coefficient, sample mass, the concentration of the i species, and sample disk area, respectively. The ε_i values for the pyridinium ions bonded to Brönsted acid sites and pyridine coordinated to Lewis acid sites were $\varepsilon_{B,Py}$ (1545 cm^{-1}) = 1.23 cm·μmol^{-1} and $\varepsilon_{L,Py}$ (1450 cm^{-1}) = 1.73 cm·μmol^{-1}, respectively**[76]**.

Transmission FTIR spectra of the samples were recorded using a Bruker spectrometer (Vertex 70) equipped with an MCT detector to register the vibrational modes over the range 3200-3800 cm^{-1} corresponding to the hydroxyl region of the IR spectra. The materials diluted in KBr (10%) were submitted in a flow Ar at 150 °C for 2 h to remove physisorbed water/moisture.

Fourier-transform infrared (FT-IR) spectroscopy was performed to characterize the functional groups spectra of the fresh and post-reaction copper catalysts within a wavenumber range from 4000 to 400 cm^{-1}. FT-IR spectra were recorded on a Nicolet Magna Infrared spectrometer using the KBr pellets method.

UV-Vis diffuse reflectance spectra (UV-Vis DRS) profiles were recorded in the range of 200-1100 nm (nominal resolution of 1 nm) by a Thermo Scientific spectrometer (model Evolution 300) equipped with a

Harrick diffuse reflection accessory (Praying Mantis) using a PTFE as a reference. The Kubelka-Munk function $F(R_\infty)$ for infinitely thick samples was used to convert reflectance measurements ($\%R$) into equivalent absorption spectra. The original data of the reflectance spectra ($\%R$) as a function of wavelength (λ) were treated with the Kubelka-Munk function and the modified Kubelka-Munk function**[77, 78]** to determine the optical absorption edge energy values (E_b) as indicated by the following equations:

$$F(R_\infty) = \frac{(1 - R_\infty)^2}{2R_\infty} = \frac{\alpha}{S} \quad \text{(Eq. 2)}$$

Where $F(R_\infty)$ corresponds to the reflectance transformed according to the Kubelka-Munk function and R_∞ is the ratio between the reflectance of the sample and the reference sample. This expression directly determines the relationship between the absorption (α) and scattering (S) coefficients and the reflectance ratio between the target sample and the reference sample, measured at an infinite penetration distance. Considering the energy-independent scattering coefficient, the Kubelka-Munk function can be assumed proportional to the absorption coefficient which is defined by the following expression:

$$\alpha = \frac{(h\nu - E_b)^\eta}{h\nu} \quad \text{(Eq. 3)}$$

And thereby the modified Kubelka-Munk Function expression is obtained:

$$F(R_\infty) = \frac{(h\nu - E_b)^\eta}{h\nu} \quad \text{(Eq. 4)}$$

$$(F(R_\infty)h\nu)^{1/\eta} = h\nu - E_b \quad \text{(Eq. 5)}$$

Where $h\nu$ is the energy of the incident photon, E_b is the optical absorption edge energy, and the exponent η depends on the type of optical transition caused by photon absorption. By plotting the modified Kubelka-Munk function $(F(R_\infty)h\nu)^{1/\eta}$ as a function of $h\nu$ (Eq. 5) and extrapolating the linear part of the curve in the low-energy region, it is possible to determine the edge energy values which provide information about the oxidation state and environment of the species involved in these optical transitions. For this study, direct transitions were considered, so η = ½.

X-ray photoelectron spectroscopy (XPS) analysis was carried out on a Kratos Axis Ultra HAS spectrometer with a hemispherical analyzer and Mg Kα X-ray radiation source ($h\nu$ = 1253.6 eV) operated at 10 mA and 15 kV. The binding energy (BE) of the sample was calibrated to the C 1*s* line (BE = 285.0 eV). The spectral data were treated using the CasaXPS software.

339 *2.3.4. Programmed temperature analyses*

340 Approximately 50 mg of sample was used for the temperature-programmed analyses. The sample was
341 loaded into a U-shaped quartz tube arranged between layers of quartz wool attached to AutoChem II 2920
342 equipment. The water formed during the programmed temperatures was removed from the gas stream in a
343 dewar with a cooling bath maintained at -10 °C.

344 For the temperature-programmed desorption of NH_3 (NH_3-TPD) experiments, the samples (ca. 50 mg) were
345 reduced at 400 °C (5 °C·min^{-1}) for 2 h in H_2 flow (20 mL·min^{-1}). Then, the sample was cooled to 40 °C with
346 Ar flow (20 mL·min^{-1}) and subsequently saturated with NH_3 flow (20 mL·min^{-1}) for 10 min at 40 °C. After
347 that, the sample was heated to 75 °C (5 °C·min^{-1}) under an Ar flow (20 mL·min^{-1}) to remove physically
348 adsorbed (weakly held) NH_3. The concentration of ammonia desorbing from the sample was continuously
349 monitored with a thermal conductivity detector (TCD). The total amount of desorbed ammonia in the
350 samples was obtained by the standardized ammonia TPD peak areas following the calibration of the TCD
351 detector.

352 In the H_2 temperature-programmed reduction (H_2-TPR) experiments, the sample was oxidized with a flow
353 of 10% O_2/He (50 mL·min^{-1}) from room temperature to 500 °C (5 °C·min^{-1}) for 30 min. Then, the sample
354 was cooled to 50 °C in flow of He (50 mL·min^{-1}) and allowed to stabilize for 10 min. After cooling under
355 He, the gas was switched to 5% H_2/Ar with a flow of 50 mL·min^{-1}, raising the temperature to 900 °C (5
356 °C·min^{-1}), and the amount of H_2 consumed was monitored by the TCD detector previously calibrated using
357 CuO reduction as reference.

358 The dispersion of Cu was measured by N_2O passivation coupled with temperature-programmed reduction.
359 The technique comprises three steps: reduction to Cu^0, oxidation of Cu^0 to Cu_2O using N_2O, and
360 temperature-programmed reduction of Cu_2O surface species. The sample was initially outgassed at 90 °C
361 under He for 1 h and then reduced with 5% H_2/He (50 mL·min^{-1}) from room temperature to 400 °C (5
362 °C·min^{-1}) for 120 min (Step 1, Eq. 6). The reduced sample was cooled in He flow (50 mL·min^{-1}) to 40 °C
363 and purged for 30 min. Then, 20% N_2O/Ar flow (20 mL·min^{-1}) was introduced to oxidate selectively the
364 surface Cu^0 species (Step 2, Eq. 7) at 40 °C for 1 h. Later, He (50 mL·min^{-1}) flowed to decrease the
365 temperature to 35 °C and stayed for 10 min. Ultimately, the reduction of surface Cu_2O to metallic Cu was
366 performed with 5% H_2/He flow (50 mL·min^{-1}) by raising the temperature from 35 to 900 °C (5 °C·min^{-1})
367 (Step 3, Eq. 8). The H_2 consumption was followed by a TCD detector. Then, copper dispersion $D(\%)$
368 defined as a ratio of Cu exposed at the surface ($Cu_{surface}$) determined by N_2O to total Cu content (Cu_{total})

369 determined by H_2-TPR analysis, was calculated by using Eq. 9, considering the stoichiometry of N_2O/CuO
370 = 0.5 mol N_2O/mol Cu^0.

$$CuO_{(s)} + H_{2(g)} \rightarrow Cu_{(s)} + H_2O_{(g)} \quad \text{(Eq. 6)}$$

$$N_2O_{(g)} + 2Cu_{(s)} \rightarrow Cu_2O_{(s)} + N_{2_{(g)}} \quad \text{(Eq. 7)}$$

$$Cu_2O_{(s)} + H_{2(g)} \rightarrow 2Cu_{(s)} + H_2O_{(g)} \quad \text{(Eq. 8)}$$

$$D(\%) = \frac{Cu_{surface}\ (\mu mol \cdot g_{cat}^{-1})}{Cu_{total}\ (\mu mol \cdot g_{cat}^{-1})} \times 100\% \quad \text{(Eq. 9)}$$

371

372 The deposits of carbon on the used catalysts were measured by temperature-programmed oxidation (TPO).
373 Previously to the experiments, the post-reaction catalyst was centrifuged, washed with deionized water to
374 remove physically adsorbed species on the surface, dried at 80 °C for 24 h, and stored in a desiccator. The
375 sample was heated from room temperature (RT) up to 70 °C (5 °C·min^{-1}) for 30 min and then cooled down
376 to RT. TPO experiments were carried out starting from RT up to 900 °C with a heating rate of 5 °C·min^{-1}
377 in a 10% O_2/He flow of 50 mL·min^{-1} after waiting for the baseline to stabilize. The amount of desorbed CO_2
378 was quantified by using a TCD with the help of a reference test, using a defined CO_2 pulse over 50 mg of
379 inert quartz.

380

381

382

383 *2.4. Catalytic test reaction*

384 The catalytic dehydration of glycerol was conducted in a Parr 5500 compact reactor with 600 mL capacity,
385 adapted to a Parr 4848 controller. Before the reaction, the copper catalyst was reduced in a quartz reactor
386 with an H_2 flow (20 mL·min^{-1}) from room temperature to 400 °C (5 °C·min^{-1}) for 4 h. The composition of
387 the reactor feed consisted of 60 g of an 80 wt%. aqueous glycerol solution (glycerol, Sigma-Aldrich, 99.5
388 %) and 300 mg of the reduced catalyst (corresponding to a glycerol/Cu molar ratio = 2205). Consequently,
389 the reactor was closed, purged with $N_{2(g)}$ to ensure an inert atmosphere, and heated with an agitation of 400
390 rpm until the temperature was 120 °C. Then, when the reactor reached 220 °C the agitation was increased
391 and maintained at 800 rpm, allowing autogenous pressure to be reached. Additional N_2 was used to achieve
392 a constant working pressure of 20 bar. Reaction time was set to 5 h and sample aliquots were collected at
393 different times. These aliquots were filtered and separated into two series: one series was analyzed by gas
394 chromatography (GC), while the other series was diluted using a dilution factor of 15 ($V_{final}/V_{initial}$) and
395 analyzed by high-performance liquid chromatography (HPLC). Glycerol consumption was analyzed on
396 YL9100 high-performance liquid chromatograph (HPLC) equipment equipped with an ICSep ICE-
397 COREGEL 87H3 column and DAD and RID detectors using an isothermic method at 40 °C with a runtime
398 of 20 min. The mobile phase was an aqueous solution of 5 mM H_2SO_4 (0.6 mL·min^{-1}). The HPLC analyses
399 of the liquid samples were used to evaluate the progress of the reaction by calculation of glycerol conversion
400 $X(\%)$ according to Eq. 10, where C_{gly}^0 and C_{gly}^t are the initial and final glycerol concentrations (expressed in
401 wt%.), at a given time t, respectively.

$$X(\%) = \frac{C_{gly}^0 - C_{gly}^t}{C_{gly}^0} \times 100\% \qquad \text{(Eq. 10)}$$

402 For the identification and quantification of the reaction products a Perkin Elmer XL Autosystem gas
403 chromatograph equipped with a Nukol capillary column (30 m × 0.53 mm × 0.5 μm) and flame ionization
404 detector (FID) was used, with He as carrier gas. The chromatograms were obtained using the following
405 temperature program: (a) 40 °C (0 min); (b) ramp of 1 °C·min^{-1} from 40 to 50 °C for 6 min; (c) ramp of 5
406 °C·min^{-1} from 50 to 160 °C, maintaining this temperature for 0 min; and (d) 10 °C·min^{-1} ramp from 160 to
407 200 °C for 18 min, giving a total runtime of 60 min. The selectivity of the products i and the yield of the
408 main products were calculated respectively based on Equations 11 and 12, where S_i is the selectivity for the
409 product i, A_i is the area under the peak determined for product i, divided by the sum of the areas of all
410 products A_j, where j takes as many values as products were identified and not identified by gas
411 chromatography, Y_i is the yield for the product i calculated as the glycerol conversion $X(\%)$ multiplied by
412 the selectivity for this product.

$$S_i(\%) = \frac{A_i}{\sum_1^\infty A_j} \times 100\% \quad \text{(Eq. 11)}$$

$$Y_i(\%) = \frac{S_i \times X}{100\%} \quad \text{(Eq. 12)}$$

The catalytic activity was expressed in terms of a specific initial reaction rate, calculated from the initial slope of the glycerol conversion curve as a function of reaction time, with the data acquired during the first 120 min of reaction guaranteeing linear behavior using the Eq. 13, where r_{gly}^0 is the specific initial reaction rate ($mol_{gly} \cdot g_{cat}^{-1} \cdot min^{-1}$), n_{gly}^0 is the initial number of mol of glycerol, s is the slope ($\% \cdot min^{-1}$) obtained from the linear fit of the first points of the curve and m_{cat} is the mass of the catalyst (g).

$$r_{gly}^0 \left(\frac{mol_{gly}}{g_{cat} \times min} \right) = \frac{n_{gly}^0 \times s}{m_{cat} \times 100\%} \quad \text{(Eq. 13)}$$

Additionally, the initial reaction rates of formation $r_{f,i}^0$ of the main products i were determined. These were calculated from the slope s obtained from the curve that represents mol of product (mol) formed as a function of reaction time (min) and normalized by the catalyst mass.

$$r_{f,i}^0 \left(\frac{mol_i}{g_{cat} \times min} \right) = \frac{s}{m_{cat}} \quad \text{(Eq. 14)}$$

3. Results and discussions

3.1. Characterization

3.1.1. Chemical composition.

Chemical analysis from ICP-MS and the near-surface composition from XPS spectra were tabulated in Table 1 together with XRF measurements. The analyses indicated that the Si/Al ratio and Cu content were close to the targeted values. This demonstrated a high efficiency in the incorporation of the Al and Cu species. However, from the XPS measurements, it can be seen that the upon introduction of Cu species, the surface composition changed.

Table 1. Elemental composition of the materials

Sample	Si/Al molar ratio nominal (gel)	Si/Al molar ratio of final sample			Cu loading (wt%)[a]
		XRF	EDS	XPS	
SBA-15	∞	n.a.	n.a.	n.a.	n.a.
SBA-15 SiAl 15	15	11.4	15.1	11.5	n.a.
SBA-15 SiAl 10	10	8.5	10.0	9.4	n.a.
SBA-15 SiAl 2	2	2.5	2.1	2.1	n.a.
Cu/SBA-15	∞	n.a.	n.a.	n.a.	5.7
Cu/SBA-15 SiAl 15	15	n.d.	n.d.	64.6	5.0
Cu/SBA-15 SiAl 10	10	n.d.	n.d.	10.1	4.8
Cu/SBA-15 SiAl 2	2	n.d.	n.d.	3.2	4.7

[a] Determined by ICP-MS
n.a.= not applicable.
n.d.= not determined.

3.1.2. Textural and Structural Properties

The N_2 physisorption isotherms and pore size distribution for copper catalysts are shown in Figure 1(a) and (b), and the estimated textural parameters for supports and copper catalysts are tabulated in Table 2. Samples gave typical type IV isotherms, representative of a typically ordered mesoporous structure with double opened cylindrical-shaped pores as consistent with literature studies**[56, 79, 80]**. It shows that the

mesoporous structure is still retained after the incorporation of heteroatoms in the matrix of SBA-15. However, it can be clearly seen that different hysteresis loops were obtained with the variation of the Si/Al molar ratio. Initially, the Cu/SBA-15 sample displayed an H1 hysteresis loop characterized by nearly perpendicular adsorption and desorption branches. It supports the existence of a large amount of uniform-size ordered mesopores in the support. Next, with the incorporation of Al (Si/Al ratio decreases) in the SBA-15, the inflection of the adsorption-desorption branches becomes less pronounced, and the hysteresis loop gradually deforms adopting an H3-type behavior. This feature is associated with a change in the shape of mesopores from cylindrical to slit-like channels**[81]**. Such aspect, as explained in our previous work**[82]**, can be attributed to the formation of parallel macropores created during the process of aluminum assembly into the structure, due to pore-blocking/percolation in a narrow range of pore necks and/or to the partial destruction of the ordered structure of SBA-15 by the formation of particle aggregates when the Al content is high**[53, 83, 84]**. This suggests that the Al incorporation would greatly impact the textural porosity, while the addition of copper slightly affected the textural properties.

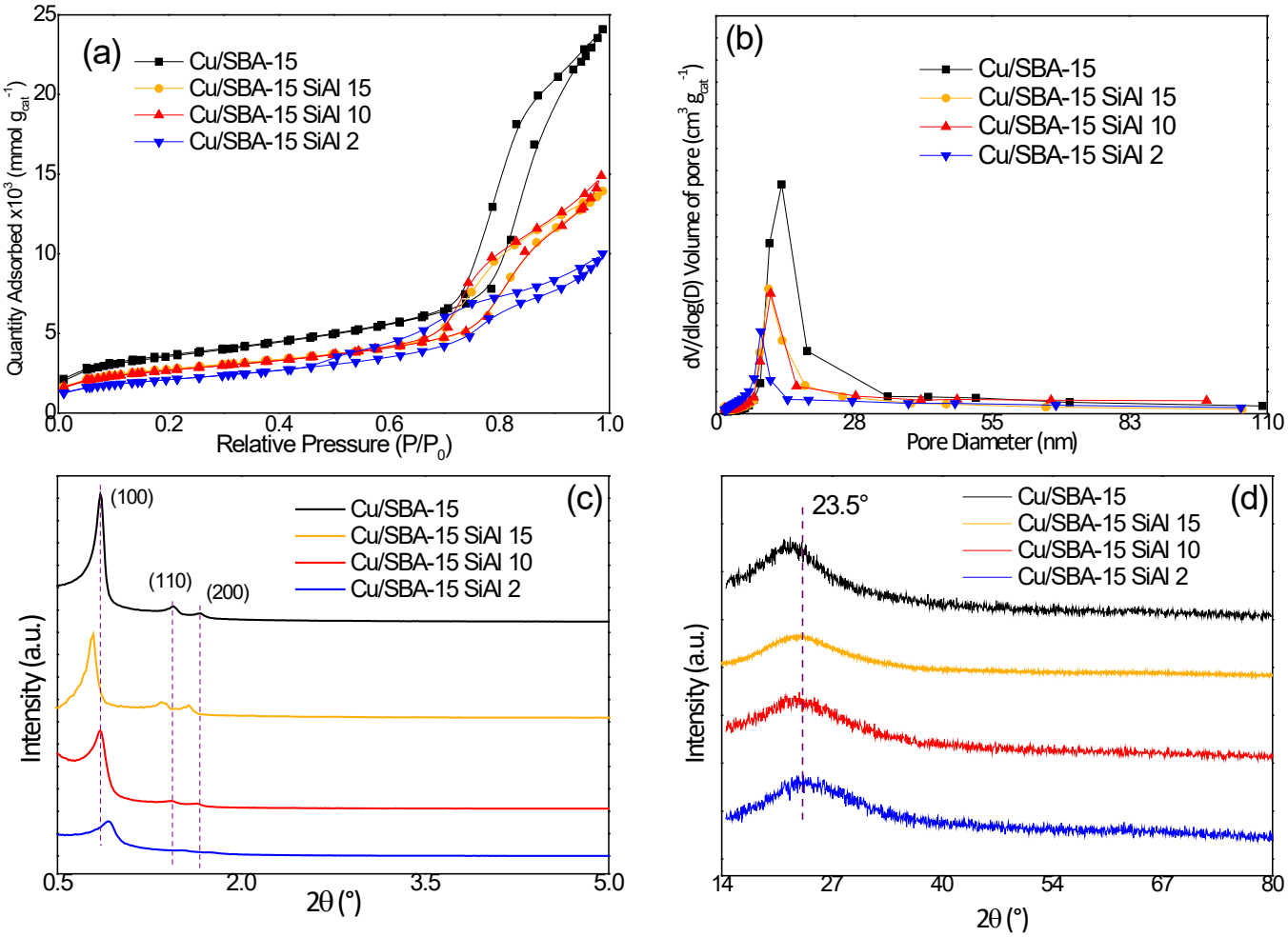

Figure 1. (a) N_2 adsorption-desorption isotherms and (b) pore size distribution curves of the materials and XRD patterns of Cu/SBA-15 samples: (c) small-angle and (d) wide-angle.

Table 2. Physicochemical properties of the synthetic materials determined by N_2 adsorption-desorption and XRD measurements.

Sample	S_{BET} ($m^2 \cdot g^{-1}$)	V_p [a] ($cm^3 \cdot g^{-1}$)	d_p [b] (nm)	d_{100} [c] (nm)	a_0 [d] (nm)	w [e] (nm)
SBA-15	525	1.10	9.8	9.4	12.2	3.9
SBA-15 SiAl 15	382	0,72	8.4	8.4	13.2	5.7
SBA-15 SiAl 10	374	0.61	8.0	8.0	13.0	6.4
SBA-15 SiAl 2	381	0.50	5.5	5.5	12.2	7.1
Cu/SBA-15	273	0.78	11.4	10.9	12.6	4.2
Cu/SBA-15 SiAl 15	208	0.44	8.5	11.4	13.2	4.7
Cu/SBA-15 SiAl 10	204	0.44	8.8	11.2	12.9	4.1
Cu/SBA-15 SiAl 2	163	0.30	7.3	10.6	12.2	4.9

[a] Pore volume calculated at $P/P_0 = 0.95$. [b] BJH desorption average pore diameter. [c] Interplanar distance of (100) reflection. [d] Unit cell parameter: $\left(a_0 = 2 \times \frac{d_{100}}{\sqrt{3}}\right)$. [e] Pore wall thickness: $w = a_0 - d_p$.

The decrease of nitrogen uptake with increased Al introduction in the SBA-15 was indicative of smaller mesopores volumes than samples that are aluminum-free. The specific surface area (S_{BET}) and pore volume (V_P) of the SBA-15 support decreased with the incorporation of Al (Table 2). Copper catalysts exhibited lower specific surface area and pore volume compared to the correspondent supports. The values of S_{BET} and V_P of the Cu/SBA-15 were 273 $m^2 \cdot g^{-1}$ and 0.78 $cm^3 \cdot g^{-1}$ (Table 2). In the prepared Cu/SBA-15 SiAl x catalysts the S_{BET} and V_P values decreased to 208-163 $m^2 \cdot g^{-1}$ and 0.44-0.30 $cm^3 \cdot g^{-1}$ compared to Cu/SBA-15 catalyst. A decrease in the specific surface area accompanied by a significant loss of the total pore volume occurs when copper is introduced in the starting supports.

The samples exhibited an unimodal pore size distribution. A decrease in the average pore size of the SBA-15 supports is also noticed with higher aluminum loadings. Meanwhile, with the addition of Cu species an increase in the average pore diameter compared with the supports. However, the pore size distribution of the copper catalysts derived by the adsorption isotherm of the BJH method also shows a decrease in size as the aluminum load increases. This would indicate that a certain amount of pores have been filled due to copper species deposition**[85]**. This is noticed from the decrease in the pore size distribution of the copper catalysts (Figure 1(b) and Table 2), where mesopores contracted from 11.4 nm for the Cu/SBA-15 to 7.3 nm for the Cu/SBA-15 SiAl 2 sample. Notably, the unique modal distribution of the pores demonstrates the homogeneous character of the mesopores.

Copper surface deposition or its insertion into the hexagonal structure of SBA-15 could be enough to block a certain number of mesopores and could lead to a decrease in the pore volume, which would result in a decrease in the S_{BET} surface**[69, 86]**. Nevertheless, the pore size shows the opposite trend. A pore enlargement compared to the supports took place after CuO loading for all samples. This phenomenon can be associated with two causes: (1) due to the dissolution of the outer silica layer in silicic acid caused by the copper incorporation method; and (2) due to an isomorphic substitution of the deeper Si atoms within the silica lattice. Each cause is explained as follows: during the ammonia evaporation method may occur dissolution of the silica walls to result in the formation of silicic acid and copper phyllosilicates. The reason lies in the absolute amount of OH^- ions in the solution, which are produced by the auto-protolysis of water by the presence of ammonia. These ions react with the silica walls, forming silicic acid ($Si(OH)_4$), which in turn reacts with the $Cu(OH)_2(H_2O)_4$ complex to form the copper phyllosilicates, which in turn gives rise to CuO species when the material is calcined**[27, 69, 87]**. Whereas if the substitution of the deeper Si atoms in the silica lattice occurred, it would lead to unit cell enlargement due to the longer length of the metal-oxygen bond, resulting in mesopore expansion**[87, 88]**. According to the literature, the higher radius of Cu^{2+} (0.070 nm) with respect to Si^{4+} (0.040 nm) and Al^{3+} (0.054 nm) ions could justify the observed mesopore expansion, due to the longer Cu–O bonds**[87, 89]**. Since the lattice parameters determined from the XRD results (Table 2) did not show a noticeable change after Cu incorporation, it is hypothesized that the increase in the average pore size is due to the dissolution of the silica walls by the ammonia evaporation method.

The low-angle XRD patterns of the copper catalysts (Figure 1(c)) were like those recorded for starting supports as reported by our previous work**[82]**. It can be seen that upon Cu introduction, no significant changes in the patterns were observed. Meanwhile, as the Al content increases, the reflections indexed to the (100), (110), and (200) planes of the hexagonal structure become less intense, confirming that the loss of structural order is attributed to the incorporation of consecutive Al loadings *via* the "pH-adjusting" method (for molar ratio Si/Al ≤ 15)**[90]**. In addition, the structural parameters do not show a considerable effect on the Cu species loading in the framework of the SBA-15. The cell parameter a_0 and d_{100} spacing values ranged around 13.2-12.2 nm and 11.4-10.6 nm respectively, which are similar to those of the initial supports (Table 2). These results suggest that the substitution of Si atoms for Al atoms in the silica lattice of the hexagonal structure of SBA-15 leads to deformation in the channel organization, which becomes more prominent as the Al loading increases. In addition, the calculated lattice parameter (a_0) of the catalyst series increases from 12.6 to 13.2 nm when the value of the Si/Al molar ratio decreases from ∞ to 15. Next, the value of the cell parameter decreases from 13.2 to 12.2 nm when the value of the Si/Al molar ratio decreases from 15 to 2. This indirectly confirms the substitution of Cu atoms in the framework of SBA-15, which is favored by the presence of Al in the SBA-15 up to a certain content. Otherwise, no significant

changes in the unit cell parameter a_0 and d_{100} spacing was noted by the incorporation of the Cu-phase (a_0 and d_{100} spacing values ranged around 13.2-12.2 nm and 11.4-10.6 nm respectively). It may be concluded that CuO particles were uniformly distributed on the surface or pore wall of the mesoporous SBA-15.

In the wide-angle region, only the diffraction signal centered at 2θ = 23.5° associated with amorphous silica is distinguishable**[91]**. Thus, the formation of any crystalline aluminum (Al_2O_3 or $Al(OH)_3$) or copper phase in the material is ruled out, suggesting then that a high dispersion of both elements occurred throughout the matrix of the mesoporous structure or that both are in an amorphous state. The absence of representative diffraction lines characteristic of copper phases suggests the formation of small copper particles below the XRD detection limit or their settling deep in the support walls**[90]**. This is consistent with the study developed by Boosa et al.**[92]** in which it is reported that at low copper contents (5% wt. Cu), CuO species are present in a highly dispersed state in this class of mesoporous materials. Then, based on the hypothesis mentioned above and the N_2 physisorption together XRD results, we believe the following: when the Cu atoms are added, it is possible that the chemical environment of the previously deposited Al on the SBA-15 structure (i.e. the lattice oxygen atoms, belonging either to the silanol groups or the aluminol groups provided by the incorporated Al species) facilitates a specific interaction with the copper species, aiming to stabilize and enhance the dispersion of the copper particles**[93]**. It is probable that the aluminum species already integrated into the SBA-15 framework form a thin layer or coating on the surface of the mesopores**[46]**. Subsequently, the introduced Cu species likely penetrate initially this Al_xO_y layer rather than the silica network, thereby minimally altering the cell parameter.

The HRTEM and HAADF-STEM images of the local structure of the catalysts are shown in Figure 2. Figure 2(a) shows that the hexagonal arrangement of the mesostructure of SBA-15 is preserved because the characteristic tubular channels along the observed copper particles are clearly distinguishable. However, the local discontinuity of the mesopores that was observed in the starting supports is due to the effect of incorporation of Al species**[82, 90]**. On the other hand, apparently, the structural order of the materials is not significantly affected by the incorporation of copper into the support. In fact, as can be seen in Figure 2(b) the Cu/SBA-15 material exhibits a well-defined tubular structure with a long range of ordering of the mesopores. Further, the Fourier Transform image inserted in this micrograph indicates that the lattice has an interplanar spacing of 10.8 nm, having correspondence with the value obtained by XRD (Table 2) and confirming that the material preserves the structural characteristics of its starting material SBA-15 at long range order. In contrast, the Cu/SBA-15 SiAl 10 and Cu/SBA-15 SiAl 2 samples (Figure 2(c) and Figure 2(e), respectively) exhibit the same decreasing range ordering that was observed in the starting materials but the hexagonal array of mesopores can still be clearly observed. A partial destruction and gradual

decrease in the extent of straight channels is observed. The materials fragment into domains that decrease in size oriented in different directions due to higher Al incorporation. The changes in the hysteresis loop shape and the decrease in the intensity of the diffraction peaks confirm the alteration of the ordered mesopore structure SBA-15 is primarily attributed to aluminum incorporation into the SBA-15 matrix, while copper plays a secondary role.

On the other hand, it is observed that the copper species were uniformly distributed on the starting supports. Figure 2(a) shows an HAADF-STEM image of the Cu/SBA-15 sample exhibiting morphology slightly different from the parent support (Fig. S1 A-B). The channel limits were not identified, suggesting that copper incorporation takes place homogeneously. The Cu nanoparticles were observed as bright dots (marked with red circles), while Figure 2(b) corresponds to an HRTEM image where the Cu nanoparticles appear as dark dots. Representative HRTEM and HAADF-STEM images of the Cu/SBA-15 SiAl 10 (Figures 2(c) and Figure 2(d)) and Cu/SBA-15 SiAl 2 (Figures 2(e) and Figure 2(f)) samples still suggest that Cu is well dispersed. These observations reveal that a high dispersion of CuO was achieved by the ammonia evaporation method. Additional micrographs of the samples are presented in Figure S1 of the supplementary material.

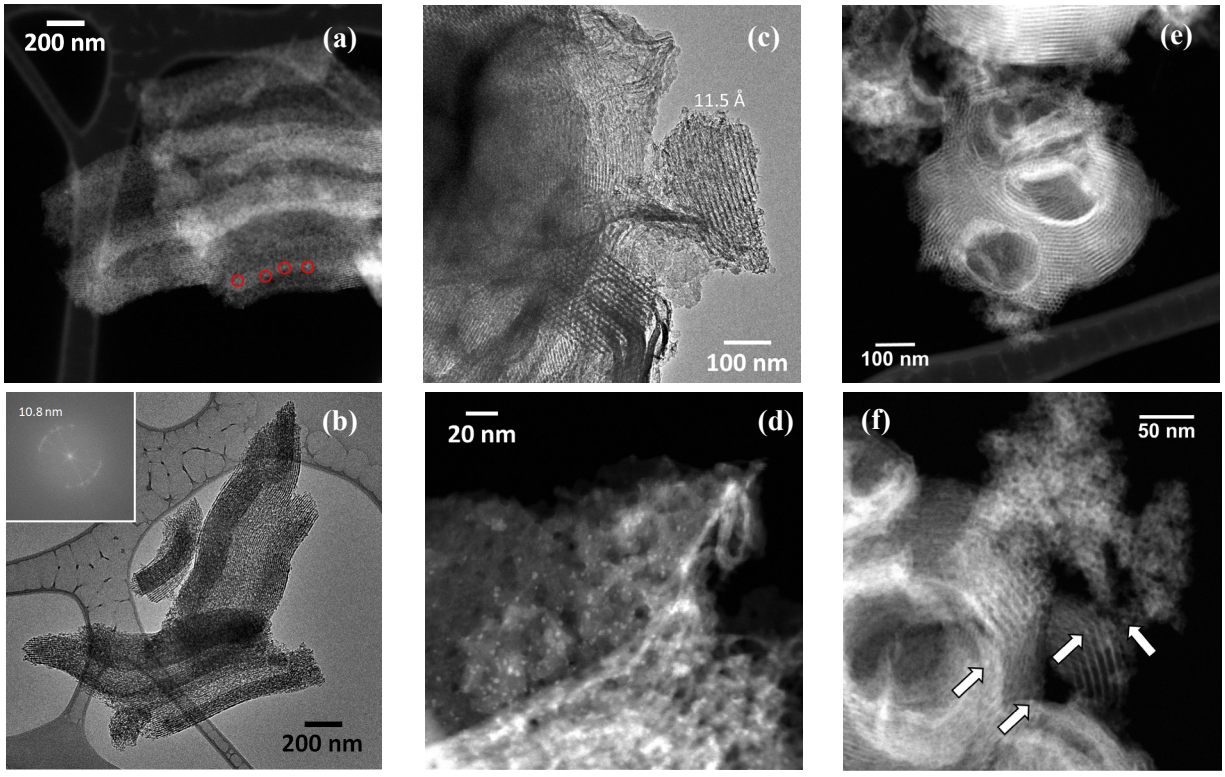

Figure 2. HRTEM and HAADF-STEM images of catalyst samples: (a) HAADF-STEM and (b) HRTEM images of Cu/SBA-15; (c) HRTEM and (d) HAADF-STEM images of Cu/SBA-15 SiAl 10 sample and (e) and (f) HAADF-STEM of Cu/SBA-15 SiAl 2 sample.

3.1.3. Temperature - Programmed (TP) Analyses

H_2 Temperature-Programmed Reduction (H_2-TPR) was used to determine the reducibility of the copper species and to study their characteristics in terms of dispersion and interaction with the support. The H_2-TPR profiles of the catalysts are presented in Figure 3(a). Bulk CuO exhibits a sharp peak at 287 °C (the inset in Fig. 3a). The reduction temperature of CuO significantly decreases after being supported on the surface of pure SBA-15. The profiles of the catalysts change with the increase in the amount of Al loading. The changes should be related to the reduction of supported CuO species in different interactions with the carrier surface, with different particle sizes, and different copper dispersion**[80, 85, 94]**. The presence of aluminum species changed the reducibility of the copper species.

The H_2-TPR profile for Cu/SBA-15 exhibited a very pronounced and almost symmetrical signal centered at 209 °C. Since XRD and HRTEM analyses suggested a high dispersion of the copper phase, this signal could be attributed to the reduction of highly dispersed copper species: isolated Cu^{2+} species and/or nano-clusters $[Cu–O–Cu]_n$ inserted in the pores of SBA-15**[95, 96]**. According to the type of synthesis adopted, the ammonia evaporation method (AE), the formation of copper phyllosilicate phases is obtained in the samples and these phases derive in highly dispersed CuO species when they decompose during the calcination treatment**[27, 30]**.

Next, as the Si/Al molar ratio in the materials decreases, in general, there is a shift of the reduction signal towards higher temperatures, accompanied by a broadening and a decrease in its intensity. This indicates a broad particle size distribution, and that the material becomes less homogeneous with increasing Al loading.

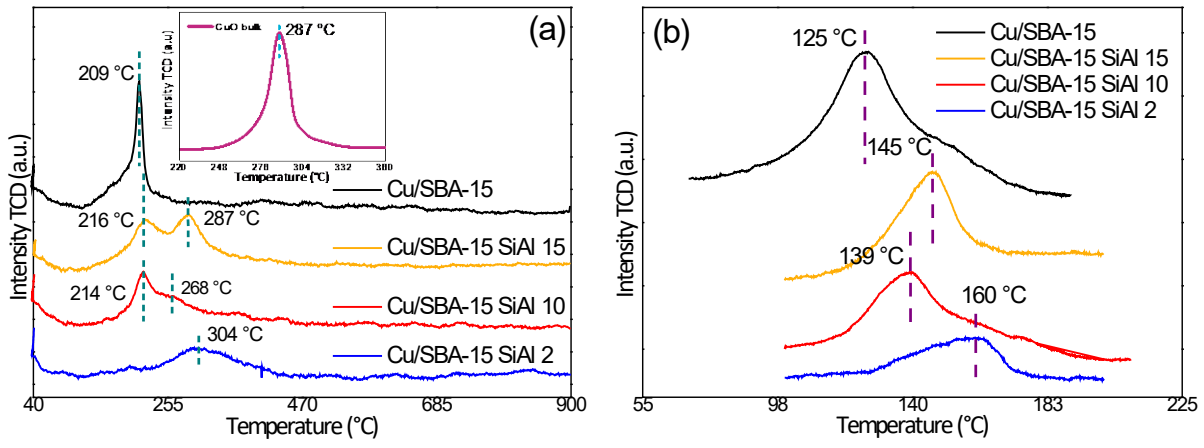

Figure 3. (a) H_2-TPR of the catalysts. The inset shows the H_2-TPR profile of CuO bulk. (b) H_2-TPR of catalysts previously passivated by N_2O

The H_2-TPR profile of the catalyst Cu/SBA-15 Si/Al 15 exhibits two very marked events shifted to higher temperatures centered at 216 °C and 287 °C, respectively. These signals could be attributed to the reduction of the Cu phase in two steps, from Cu^{2+} to Cu^{+} and from Cu^{+} to Cu^{0}, or due to the reduction of well-dispersed copper oxide species with a moderate and strong interaction with the support, respectively. Meanwhile, the profile of the Cu/SBA-15 Si/Al 10 sample shows a peak at 214 °C and a weak shoulder peak with maxima at 268 °C that could be attributed to highly dispersed Cu^{2+} species and larger CuO particles, respectively. The most complex profile belongs to Cu/SBA-15 SiAl 2 with a less pronounced, broader signal and a maximum peak reduction temperature (T_{max}) shifted towards a higher temperature (304 °C). The broadening of the signal and the shift toward high temperature may be explained by the strong metal support interaction and the formation of large clusters of CuO on the support. It should be noted that the peak tends to broaden as the Al content increases, implying that the presence of higher Al loading would be detrimental to the dispersion of copper species. The H_2-TPR profiles of catalysts previously passivated by N_2O (Figure 3(b)) followed the same tendency (discussed below). These results correlate with the metallic copper surface area measurements by N_2O chemisorption.

It is presumed that when copper is introduced into the SBA-15 and Al-SBA-15 materials, the copper species end up present in different environments when the aluminum content in the material varies. In the first instance, when copper is added to pure SBA-15, it is more likely to be deposited inside the mesoporous walls and easily dispersed along the mesostructure of SBA-15 along with some substitution of Si^{4+} ions in the matrix, as suggested by the data extracted from the physisorption and XRD techniques. In this condition the copper is forced to be embedded and confined in the structure of the SBA-15 support, leading to the formation of copper phyllosilicates during the synthesis step, which are subsequently transformed into CuO particles of reduced size after the calcination process of the sample**[83]**. In contrast, in the aluminum-containing SBA-15 supports, copper can be located in a different chemical environment, as it establishes new types of interactions with the aluminum atoms that were previously incorporated into the material. That is, as the proportion of Al increases, a higher level of coating of the SBA-15 surface and filling of the mesopores is caused by the introduced Al species. In this context, the electronic distribution state of the mesoporous surface changes, and a fraction of the introduced copper species will not be strictly forced to be embedded and confined in the structure of the support since these species will have less possibility to access the SBA-15 matrix. It can be inferred that copper species will preferentially establish a stronger

interaction with the aluminum species present in the surface layer of the support than with the available silanol groups themselves**[46]**. Thus, it can be presumed that Cu is present in the form of larger extra-porous CuO aggregates as the aluminum content increases. In short, the complexation of Cu^{2+} ions occurs in different environments, inducing as a result a change in the dispersion and electronic features of the Cu particles.

The N_2O passivation/H_2-TPR method was used for the estimation of Cu dispersion. Similar behavior to the H_2-TPR profiles was observed and the result showed that the Si/Al ratio has a great influence on the dispersion of copper. A shift of the reduction signal towards higher temperatures as the Si/Al molar ratio decreases was observed (Figure 3(b)). The obtained data showed that the incorporated copper species were well dispersed in the mesostructured support. A higher reduction temperature is associated with a higher energy requirement for the reduction of Cu species, which is directly correlated to a stronger metal-support interaction. As the Al content in the sample increases, the copper dispersion percentage (D_{Cu} (%), Table 5) decreases, translating into an increase in particle size. From these results it is possible to suggest that the Al would be interacting and anchoring the Cu species that were deposited in the material. This effect is more prominent at the Si/Al 15 molar ratio due to the accentuated shift of the reduction signal observed in the H_2-TPR profile after passivation with N_2O**[97]**. Following this, at Si/Al < 15 molar ratios, the formation of larger particle size clusters is promoted.

3.1.4. Acidity

NH_3-TPD profiles of the SBA-15 supports and copper catalysts are shown in Figure S2. Table 3 lists the total acidity values corresponding to both series of samples (supports and catalysts) determined from the deconvolution of the NH_3-TPD profiles within the temperature range of 80-350 °C. The surface acidity of the samples is enhanced when copper species are incorporated. The total acidity values had a noticeable increase in the presence of copper, which is explained due to acidic sites contributed by ionic copper species**[92, 98]**. This is clearly evidenced by comparing the NH_3-TPD profile of the SBA-15 sample with that of the Cu/SBA-15 sample. The corresponding ammonia desorption is respectively increased from 253 to 990 $\mu mol \cdot g^{-1}$ (Table 3).

Lower total acidity was noticed for Cu/SBA-15 SiAl 15 and Cu/SBA-15 SiAl 10 compared to the Cu/SBA-15 sample. This can be attributed to the deposition of Cu species on the acidic centers of the Al species on the SBA-15 walls. On the other hand, an increase in the total acidity is evidenced for the support and the

catalyst with a Si/Al molar ratio of 2. The presence of a higher Al loading may generate segregated Al species on the SBA-15 matrix. Aluminum species also affect the Cu species availability on the catalyst.

Pyridine adsorption measurement coupled with FTIR spectroscopy (Py-FTIR) was used to detect the presence and nature of acid sites on the catalysts. The Py-FTIR spectra of the calcined catalysts are shown in Figure 4(a). All the samples showed bands at 1450 and 1610 cm^{-1} and at 1547 and 1619 cm^{-1} corresponding to the ring deformation mode of pyridine for Lewis and Brönsted acid sites, respectively. It is worth mentioning that the signal intensity of Lewis acid sites predominates in all the catalysts and gradually increases with increases in Al loading, as revealed by the quantification of the sites listed in Table 3.

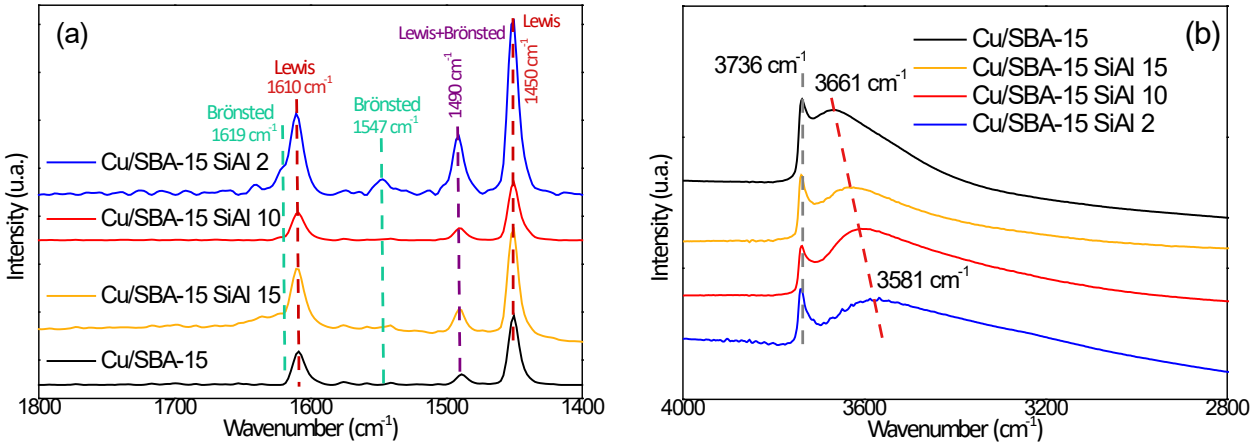

Figure 4. (a) FTIR spectra of pyridine adsorbed on Cu/SBA-15 modified with different aluminum contents. (b) FTIR spectra of each catalyst sample in the OH region.

The Brönsted to Lewis acid site ratio is another parameter that is listed in Table 3. It can be highlighted that the catalyst with the Si/Al = 2 ratio is the only one that presents, in a very low portion, Brönsted acid sites. This is attributed to the fact that Cu is deposited on the Brönsted acid sites resulting from the Al species incorporated in SBA-15. The proportion of these Brönsted sites increases with decreasing Si/Al molar ratio. Therefore, at low Si/Al ratios, the number of Cu species deposited does not cover all the acid sites present on the support surface. In comparison with the supports, it is observed that the concentration of acid sites increases after copper incorporation, in line with the evolution of the total acidity measured by NH_3-TPD. On the contrary, the intensity of the bands corresponding to Brönsted acid sites decreased. Then, the acidity of the surface of the studied catalysts is associated with the presence of Lewis acid sites and it is possible to indicate that the incorporation of copper in the supports led to an increase in Lewis's acidity. The origin of the surface Lewis acid sites due to Cu incorporation in the silica framework is linked to the local

environment of the isolated $Cu^{\delta+}$ species, that is, the type of interaction established by the Cu species with the silica structure**[95, 99]**. These differences in the contributions of the absorption bands indicate that the incorporation of copper into the siliceous structure of SBA-15 generates surface Lewis's acid sites and clearly the Cu species are mainly distributed in the Brönsted acid sites generated by the Al species incorporated into the SBA-15 matrix.

Table 3. Measurements of acidity by NH_3-TPD and Py-FTIR.

Sample	Total acidity by NH_3-TPD ($\mu mol \cdot g^{-1}$)	$C_{Brönsted}$[a] ($\mu mol \cdot g^{-1}$)	C_{Lewis}[b] ($\mu mol \cdot g^{-1}$)	$C_{Brönsted/Lewis}$[c]
SBA-15	253	0	0	u.d.[d]
SBA-15 SiAl 15	351	21	7	3.0
SBA-15 SiAl 10	202	1	3	0.3
SBA-15 SiAl 2	844	67	43	1.6
Cu/SBA-15	990	0	59	0
Cu/SBA-15 SiAl 15	772	0	79	0
Cu/SBA-15 SiAl 10	764	0	45	0
Cu/SBA-15 SiAl 2	1629	20	121	0.2

[a] Concentration of Brönsted acid sites. [b] Concentration of Lewis acid sites. [c] Ratio of Brönsted-Lewis acid sites. [d] u.d.: Undefined.

FTIR spectroscopy analyses were carried out in the region of the hydroxyl groups. Figure 4(b) shows the spectra corresponding to this region of this series of calcined catalysts. According to the reported in the literature, the band at 3736 cm^{-1} can be attributed to the stretching vibration of the isolated groups of terminal silanols**[66, 100]**, while the tail at low frequency around 3661 cm^{-1} can be assigned to the interaction between the vicinal hydroxyl groups by hydrogen bonding (-OH), being indicative of the perturbation of the Si-OH sites**[95]**. It should also be noted that this component is much more pronounced in the material with a lower Si/Al molar ratio (SiAl 2), suggesting the presence of hydroxyl groups in Al species partially embedded outside the SBA-15 matrix. However, these Al-OH species normally absorb in the region of 3700-3650 cm^{-1} and overlap with the bands corresponding to silanols linked by hydrogen bonds, making them very difficult to detect. Based on this disturbance visualized in the silanol groups, it is also possible to substantiate the creation of the acid sites in these materials detected by the previous analyses. Supported in the Hensen et al.**[101]** work, the substitution of Al species in SBA-15 generates a disturbance of the chemical environment of the siliceous network, enhancing the formation of acid sites of different nature through the formation of hydroxyl bridging groups with isolated hydroxyl sites which are present in high abundance on the surface of SBA-15. In addition, it can be inferred that the coordination environment of the Al species intervened in the anchoring of the copper species in the material, by creating structural defects

as suggested by the distortion of the silanol nests observed with the incorporation of Al in the material**[102, 103]**.

3.1.5. UV-Vis DRS

The UV-Vis DRS were recorded in order to identify and characterize the coordination environment of Cu species in intra- and/or extra-network positions in the mesoporous catalysts. Figure 5 displays the UV-Vis DRS spectra of the calcined copper catalysts. According to the literature data**[69, 87, 104]**, bands in the region between 200-400 nm (6.2-3.5 eV) can be related to mononuclear $Cu^{\delta+}$ cations in possible coordination with the oxygens of the mesoporous network of the SBA-15 material. Bands corresponding to the region 400-600 nm (3.5-2.1 eV) are assigned to linear chains of linear oligonuclear nanoclusters $[Cu–O–Cu]_n$ inserted inside the SBA-15 mesopore channels, while bulk-like segregated species of CuO in the siliceous structure are related to bands appearing between 600-800 nm (2.1-1.5 eV). The latter must correspond to d-d spin-allowed $^2E_g \rightarrow {}^2T_{2g}$ transitions of Cu^{2+} ions in a distorted octahedral environment.

Taking SBA-15 as a reference (Fig. S3 and Fig. 5(a)), the signal characteristic of pure mesoporous silica (~226 nm), according to literature studies**[98, 105, 106]**, appears weaker in the Cu/SBA-15 sample. This might suggest that the incorporation of Cu^{2+} ions occurs. Moreover, the absence of any additional band in the region between 400-800 nm suggests that this catalyst is free of copper oxide oligomers or copper clustered species, so it is inferred that the Cu species were fully dispersed in the mesoporous silica.

For samples Cu/SBA-15 SiAl 15 and Cu/SBA-15 SiAl 10 (Figure 5(a)), a more intense and broader absorption band with a shoulder is observed, whose maxima are at 219 and 337 nm, respectively. The band at 219 nm can be ascribed to surface Cu^{2+} species and charge transfer transitions between mononuclear Cu^{2+} and surface oxygen ($Cu^{2+} \leftarrow O^{2-}$) with octahedral geometry, where the copper ions occupy isolated sites over the support**[98, 107]**. While the weak band located at 337 nm could be attributed to the presence of oligomeric species $[Cu–O–Cu]_n$ in a highly dispersed state, which is not detectable by XRD. These oligomeric species are possibly inserted within mesoporous channels. Considering that the spectrum of the Cu/SBA-15 SiAl 15 sample presents a more intense band, it is presumed that under this Al loading the isolated Cu species predominate. Next, the weak behavior of the peak intensity for Cu/SBA-15 SiAl 10 and Cu/SBA-15 SiAl 2 may be due to the adhesion of Cu species to the silica wall or the Al framework**[105]**. Additionally, these materials presented a very weak band around 613 nm, which is associated with d-d transitions of Cu^{2+} ions in a pseudo-octahedral environment (CuO particles) in the extra-framework position**[87]**. In contrast, the spectrum of the Cu/SBA-15 SiAl 2 sample has much broader and weaker bands

in the region between 210-450 nm and has a larger contribution from the band at 613 nm. The presence of this contribution suggests that at high Al loadings, the formation of sintered heteroatom species is promoted.

The Kubelka–Munk plots of the copper catalysts and the band gap energy E_b (eV) are shown in Figure 5(b)-(e). The position of the absorption edge in the DRS spectra allows for estimating the particle size of the metal**[108]**. The shape and size of copper oxide particles influence the optical band gap. According to previous studies, the edge energy for CuO lies between 1.17-1.35 eV**[107]**, suggesting that the Cu species are more dispersed on the supports SBA-15 and Al-SBA-15 due to their elevated edge energy values compared to bulk CuO. Besides, this provides evidence that the introduction of the copper particles in the framework SBA-15 improves the electrical properties and the semiconducting behavior of the materials, which may lead to an increase in electron donor density**[93, 109]**.

As can be seen from the plots (Figure 5 (b)-(e)), the position of the absorption edges was shifted towards the visible region as the Si/Al molar ratio of the samples decreased. The progressive decrease in the edge energy of the aluminum-containing catalysts compared to its Cu/SBA-15 counterpart indicates an improvement in free electron density**[93]**. This shift towards low energies indicates that Cu–Cu interactions increase as the amount of Al in SBA-15 rises. This may be due to charge delocalization because of the interaction of Al species present on the support with Cu species. In other words, high Al loadings promote the segregation of Cu species and the lateral interactions between oligomers, resulting in a slight increase in the domain size of Cu species compared to the material Cu/SBA-15**[107, 108]**.

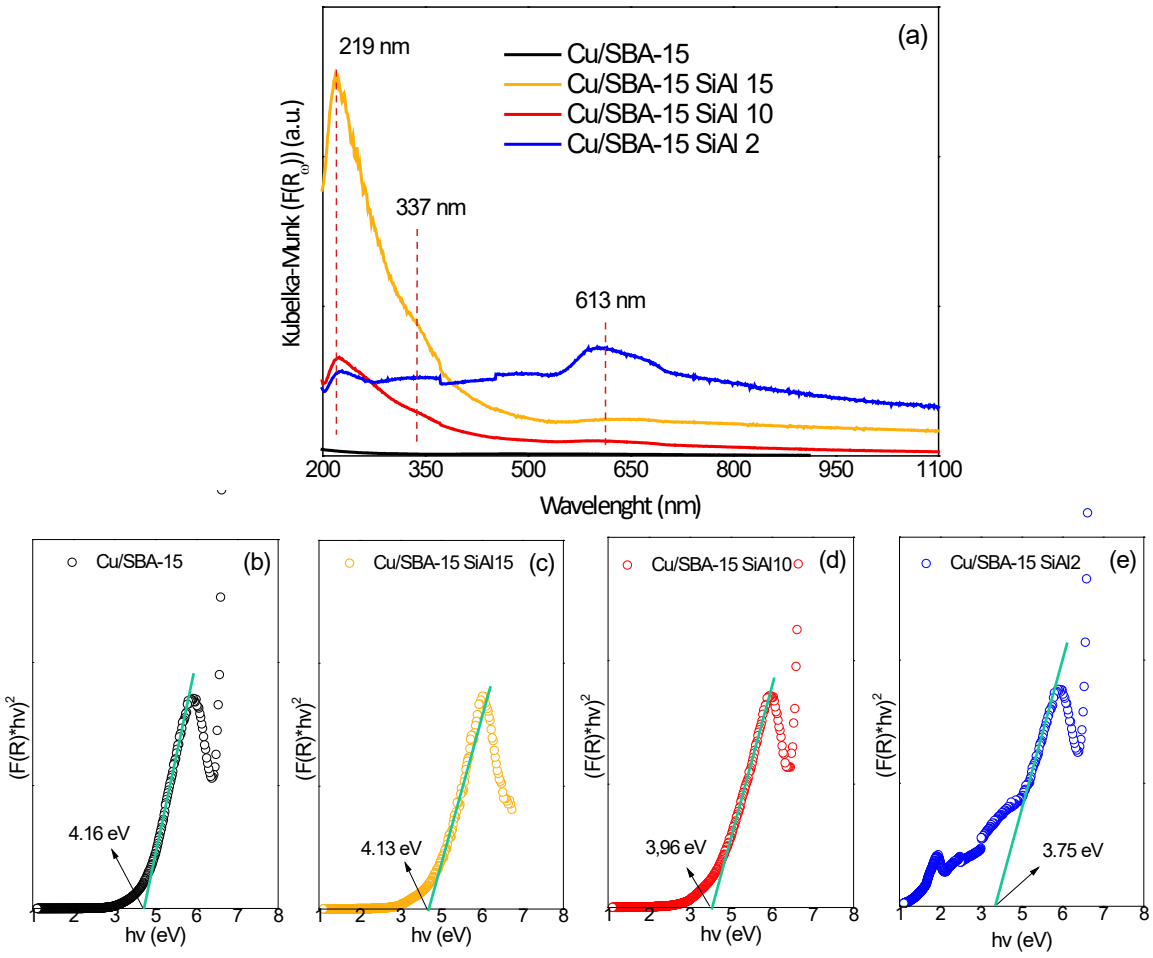

Figure 5. (a) UV-Vis diffuse-reflection spectra of copper catalysts. Kubelka-Munk plot of copper samples (b) Cu/SBA-15; (c) Cu/SBA-15 SiAl 15; (d) Cu/SBA-15 SiAl 10; (e) Cu/SBA-15 SiAl 2.

This, together with the Py-FTIR and FTIR OH region results suggest that for the Cu/SBA-15 material, part of the copper species is deposited blocking the silanol groups (Si–OH) after condensation of the copper species, leading to the formation of mononuclear Cu^{+} ions via Si–O–Cu bonds, namely by the low intensity of the absorption band at 3736 cm^{-1}; while another fraction is probably localized at terminal positions (Cu–OH species). At the same time, there are Cu species in the SBA-15 lattice bound to four lattice oxygen atoms, due to the presence of the pyridine adsorption band (1610 cm^{-1}) assigned to Lewis acid sites**[96]**. Similarly, it is possible to propose an evolution in the distribution of copper species as the Al content in SBA-15 increases, as shown in Scheme 1. The difference is that by increasing Al loadings, the formation of oligomeric Cu species and a distorted octahedral coordination environment is promoted, giving rise to nests of distorted silanols and aluminols (band broadening at 3581-3661 cm^{-1}) and acid sites of different nature (Py adsorption bands associated to Lewis and Bronsted acid sites).

The interaction between Al framework and Cu^{2+} via oxygen bridging allows the Cu species to localize on the network oxygen leading to the formation of [Si–O–Cu–O–Al] groups**[99]**. Depending on the Al content, copper ions are either embedded in the SBA-15 lattice as linear oligomeric species $[Cu–O–Cu]_n$ in a highly dispersed state as well as agglomerate to form fractions of occluded or segregated Cu species (nearest CuO neighbors) with octahedral or pseudoctahedral symmetry due to the Al species with an octahedral environment present on the surface.

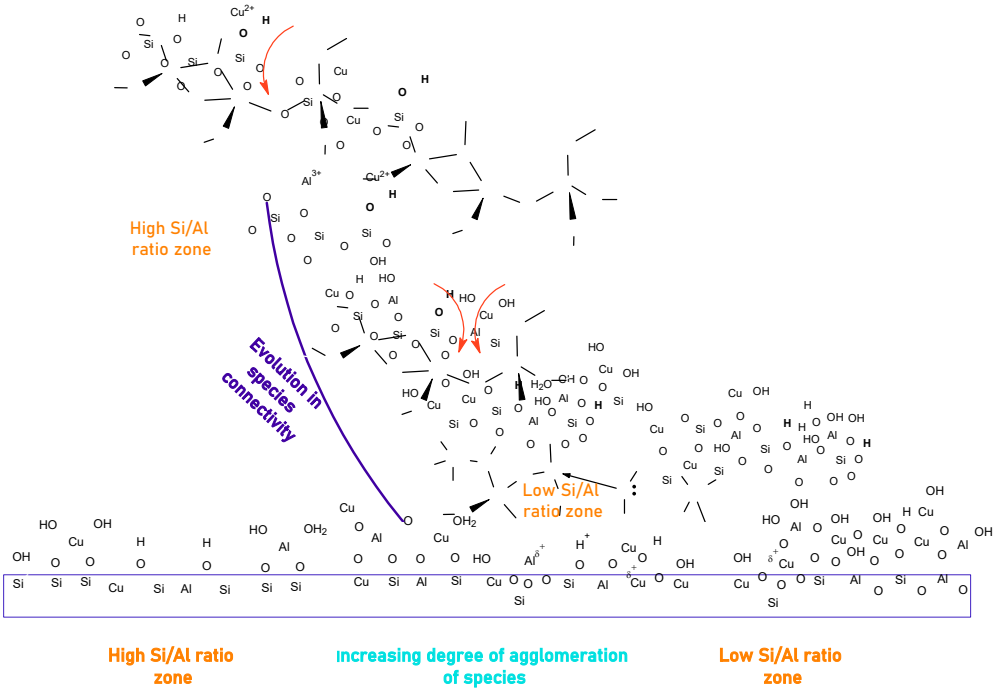

Scheme 1. Schematic representation of the SBA-15 surface, evolution of species with decreasing Si/Al ratio: silanol groups, isolated Cu species, bridging hydroxyl groups, aluminols, oligomeric copper species.

3.1.6. XPS and ^{27}Al-MAS-NMR characterization

In order to study the surface composition of the materials, XPS spectra were performed on the calcined samples. The wide and core level XPS for all the elements were calibrated for surface charging by referencing C 1s binding energy (BE) peak at 285.0 eV. Figure S4 shows the survey spectra of the copper catalysts depicting the presence of Si, O, Al, and Cu.

The XPS spectra of the Si 2p, O 1s, Al 2p, and Cu 2p levels for the catalyst series are shown in Figure 6. All binding energies are summarized in Table 4. In general, for the calcined samples, the XPS spectra of the Cu 2p level (Figure 6(a)) exhibited non-deconvoluted Cu $2p_{3/2}$ and Cu $2p_{1/2}$ peaks at ca. ~933.3 and ~953.0

884 eV with spin-orbit coupling energy of about 20.0 eV. There is no evidence of any peak at BE values below
885 933.0 eV characteristic of Cu^{+} or Cu^{0} species**[80, 99]**. This is because the samples were not exposed to a
886 reducing atmosphere. Moreover, although weak in intensity, the presence of the associated shakeup satellite
887 peaks could confirm the presence of Cu^{2+}**[110, 111]**. The absence of a peak located at 932.4 eV confirms
888 the absence of bulk copper oxide nanoparticles, in line with XRD and TEM observations**[80]**. Here, the BE
889 values of the non-deconvoluted peak of Cu $2p_{3/2}$ orbital are slightly lower than that of pure CuO (~933.8
890 eV) reported in the literature but higher than those reported in the literature for Cu_2O (933.0 eV)**[111, 112]**.
891 Thus, it is possible that the valence state of Cu is between +1 and +2. For a better analysis of the spectra,
892 the broad Cu $2p_{3/2}$ peak has been deconvoluted into two components.
893
894 Figure 6(b) shows the deconvolution of the broad Cu $2p_{3/2}$ signal in two components, revealing the presence
895 of different copper environments. The BE values of each contribution are listed in Table 4. For all samples,
896 the first component is located around 933.3-933.9 eV. This contribution is indicative of the presence of Cu^{2+}
897 species. Meanwhile, the position of the second component is around 935.5-935.9 eV, which suggests a
898 charge transfer from metal ions toward the support, i.e. Cu^{2+} species in strong interaction with the
899 support**[113]**. The peak observed at 935.8 eV in the Cu/SBA-15 catalyst is ascribed to Cu species in a high
900 degree of dispersion by the formation of Cu–O–Si–O– linkages**[20]**. Next, with the presence and increasing
901 Al loading in SBA-15 (for the samples Si/Al = 15 and Si/Al = 10), there is a lower contribution of the first
902 component, and the contribution of the second component was increased (935.9-935.5 eV). After, at Si/Al
903 = 2 the intensity of the first component (933.3 eV) increases again at the expense of the decrease of the
904 second component. In turn, the largest shift in the position of both components towards high BEs was
905 observed with the Si/Al = 15 ratio (Figure 6(b)).
906
907 These observations may suggest that with the Si/Al = 15 and Si/Al =10 ratios a higher formation of Cu
908 species in a higher oxidation state, in strong interaction with Al species and the support, is promoted**[113,**
909 **114]**. The subsequent decrease in the binding energy values of both components and increase of the
910 contribution of the first component observed with the Si/Al = 2 ratio, might be indicative of charge transfer
911 from the support matrix to the copper species since there are more Al octahedral species to compensate for
912 the charge disturbance generated by the copper species, possibly through $Al^{(Oh)}$ –O–Cu–O–Si–O bonds**[20,**
913 **113]**. As indicated in our previous work**[82]**, the XPS results revealed that the Al species would be giving
914 up their electron density to the Si and O atoms that constitute the SBA-15 matrix. Then, the Al species in
915 this configuration could transfer electron density to the Cu species.
916

Complementarily, the Cu LMM parameter can be used to differentiate the oxidation state of copper species. In this regard, the analysis of the modified Auger parameter (α) was reported by other authors**[115]** to evaluate this difference in status**[116]**. The values of the modified Auger parameters, α_{Cu}, of 1849.9 and 1849.7 eV obtained for the spectra of the catalysts Cu/SBA-15 SiAl 15 and Cu/SBA-15 SiAl 10 respectively (Table 4), corresponding approximately to the value of 1849.2 $\pm$ 0.3 eV which is attributed to the Cu_2O species**[117]**. This confirms the existence of interaction between the Cu species and the Al species whose differences between the binding energies of the catalysts become more prominent at Si/Al molar ratio values of 15 and 10. So, it is possible that Cu atoms are surrounded by Al species in the aluminum-containing samples, most likely in the structure of Cu–O–Al–O–Si upon the incorporation of copper ions into the framework of SBA-15. Possibly an interaction between Cu and especially with intra-lattice Al species induces a transfer of the electron density from Al to Cu, leading to a decrease in the Cu 2p binding energy.

On the other hand, the position of the O 1s and Si 2p peaks shifts slightly toward the low binding energy region with decreasing Si/Al molar ratio, but the XPS profile and the energy value of Al 2p does change substantially.

The deconvolution of the O 1s peak presented three contributions (Figure 6(c)). The positions and intensities of these contributions varied with the presence of Al. The first band with the lowest binding energy value is assigned to oxygen in copper oxide**[111]**. The second band can be attributed to oxygen in silanol groups. While the third band, which presents the highest binding energy value, can be attributed to oxygen in the silica structure**[111]**.

Considering the binding energies observed for the Si 2p orbital peak shown in Figure 6(d), it is observed that the Cu/SBA-15 catalyst shows a binding energy of 103.9 eV (Table 4), which is attributed to silicon oxide in a tetrahedral structure, very similar to the values reported in the literature**[118]**. Compared to Cu/SBA-15, the Si 2p binding energies of the Al-containing catalysts shift to a lower value and decrease in intensity, except for the Cu/SBA-15 SiAl 15 catalyst which recorded a slightly higher value. The latter increase can be associated with the charge imbalance associated with the interaction between the Cu and Al species**[119]**. The catalysts with Si/Al molar ratios 10 and 2 presented binding energy values of 103.1 and 103.0 eV respectively (Table 4). The shift can be attributed to the growth of a new silicon environment, due to the presence of Al(Oh) atoms which electronically perturb the silicon atoms by induced dipoles mediated via the bridging oxygen**[46, 120]**.

For the XPS spectra of the Al 2p level (Figure 6(e)), a remarkable signal evolution was observed. The XPS Al 2p spectrum of the Cu/SBA-15 SiAl 15 catalyst shows a non-deconvoluted signal centered at 78.3 eV. On the other hand, the Cu/SBA-15 SiAl 10 spectrum presents two signals, a main peak positioned at 74.2 eV and its shoulder at 77.7 eV. While in the Cu/SBA-15 SiAl 2 sample, the main signal is centered at 75.0 eV with a shoulder at 76.6 eV.

The gradual shift of the binding energy of the Al 2p peak can be attributed to the following: Aluminium present in SBA-15 at Si/Al molar ratios 15 and 10 was found prevailingly in a tetrahedral coordination environment (Figure S5). These species have an asymmetric electron density distribution around the aluminum nucleus (higher chemical shift value in ^{27}Al-MAS-NMR)**[121]**. Thus, when Cu species are introduced, the chemical state of some Al^{3+} species increases to a higher oxidation state $Al^{3+\delta}$ in order to compensate for the local charge imbalance produced by the Cu species (electrical field gradient generated by neighboring Cu species)**[39, 119, 122]**. Meanwhile, at Si/Al < 10 molar ratios, Al species exist on the SBA-15 surface in an octahedral environment, so the local charge compensation effect is diminished as there is a symmetric electron density distribution around the aluminum core and hence they have a lower binding energy. The high binding energy value observed at Si/Al = 15 molar ratio can also be attributed to a better interaction with the copper species, leading to a decrease in the electron density of the aluminum ions.

In summary, the XPS results suggest that the incorporation of progressive amounts of Al leads to the creation of a new chemical environment in the SBA-15 matrix which electronically perturbs the Cu atoms**[120]**. The remarkable change in BE of copper species in the presence of Al in the Cu/SBA-15 SiAl 15 catalyst suggests a more significant interaction effect between copper and aluminum species.

Table 5 summarizes the binding energy values for Al, Si, O, and Cu, and the estimated surface Si/Al, Cu/Si, Cu/Al, and Cu/(Si+Al) atomic ratio compositions from XPS for the samples. The Si/Al surface ratio detected by XPS decreased by increasing the aluminum loading. The Cu/(Si+Al) surface atomic ratio values (Table 5) suggest a greater amount of copper species on the catalyst surface. The Cu/(Si+Al) ratio becomes larger the greater the aluminum load. This indicates the enrichment of copper species on the surface of the catalysts**[123]**. An implicit reasoning when examining the greater amount of surface copper can be supported by the degree of agglomeration of the copper species inside the pores of the mesoporous matrix of SBA-15. The analysis of the programmed thermal reduction of H_2 of the catalysts passivated with N_2O

(Figure 3(b)) makes explicit the effect of aluminum species loading on the dispersion of copper species. In this context, the Cu/SBA-15 SiAl 2 catalyst has the lowest dispersion with a value of 26.2% (Table 5).

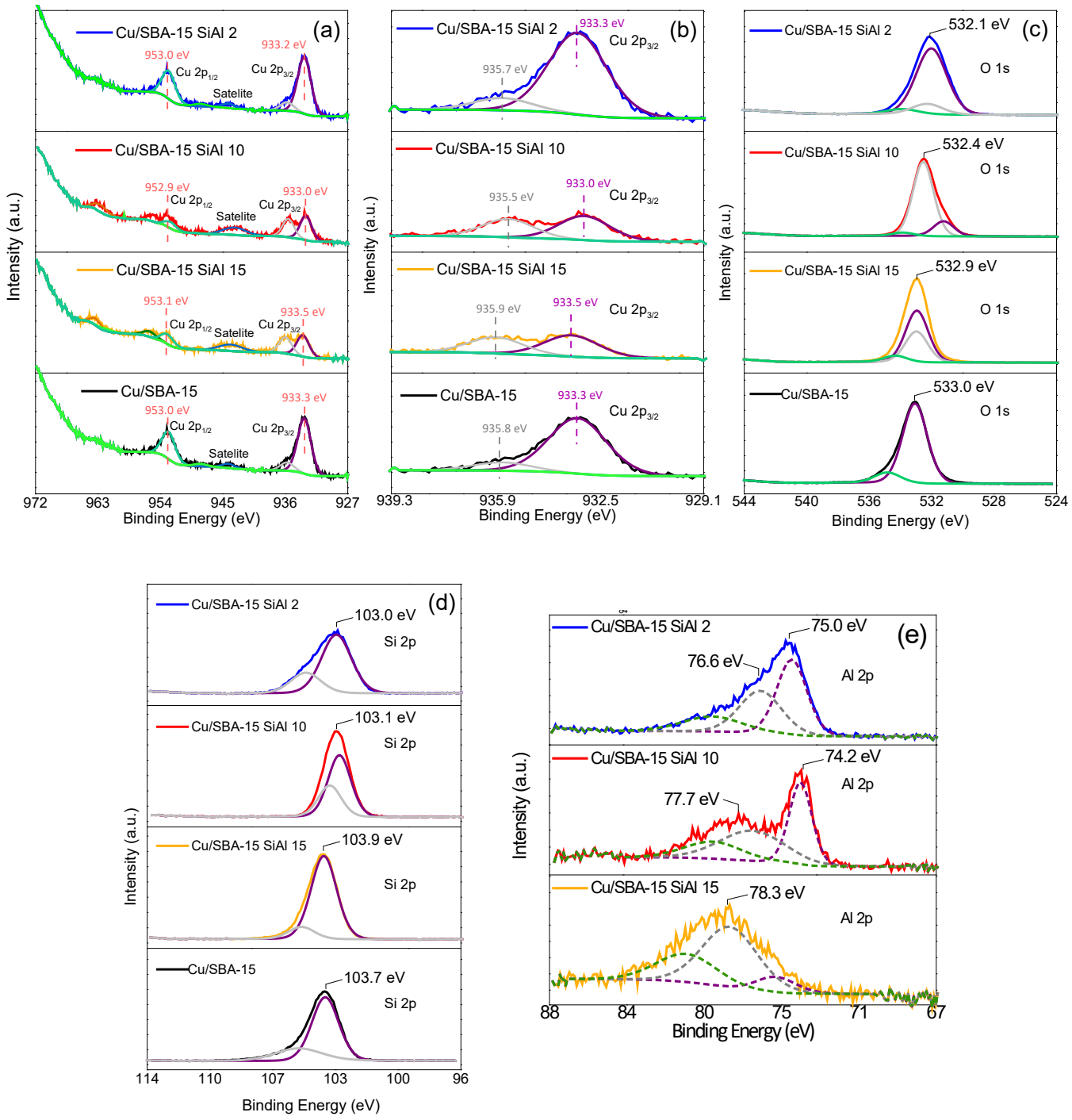

Figure 6. (a) Cu 2p core level photoelectron profile and high-resolution XPS spectra of the orbitals (b) Cu $2p_{3/2}$, (c) O 1s, (d) Si 2p, and (e) Al 2p for the catalyst series.

Table 4. Binding energies values of the Al 2p, Si 2p, O 1s, and Cu $2p_{3/2}$ orbitals.

Sample	Binding energy (eV)							
	Non-deconvoluted peak				Deconvoluted peak			
	Al 2*p*	Si 2*p*	O 1*s*	Cu $2p_{3/2}$	Cu $2p_{3/2}$		Cu LMM	α_{Cu}[a] (Auger)
Cu/SBA-15	n.d.	103.8	533.0	935.6	935.8	933.3	916.2	1851.8
Cu/SBA-15 SiAl 15	78.3	103.9	532.9	933.4	935.9	933.5	916.3	1849.7
Cu/SBA-15 SiAl 10	74.2	103.1	532.5	933.0	935.5	933.0	916.9	1849.9
Cu/SBA-15 SiAl 2	75.0	103.0	532.2	933.4	935.7	933.3	916.7	1850.0

[a] Auger parameter α = binding energy of Cu$2p_{3/2}$ + kinetic energy of Cu LMM.

Table 5. Surface atomic ratio of different elements and copper dispersion in the copper catalysts.

Sample	Surface atomic ratio				N_2O /H_2-TPR
	Si/Al	Cu/Si	Cu/Al	Cu/(Si+Al)	D_{Cu}(%)
Cu/SBA-15	n.a.	0.666	n.a.	n.a.	84.4
Cu/SBA-15 SiAl 15	64.6	0.022	1.40	0.021	48.7
Cu/SBA-15 SiAl 10	10.1	0.030	0.30	0.027	51.0
Cu/SBA-15 SiAl 2	3.2	0.047	0.15	0.036	26.2

n.a.: not applicable.

3.2. Catalytic Performance

3.2.1. Effect of Si/Al molar ratio on glycerol dehydration

The glycerol conversion profiles as a function of reaction time for this series of catalysts are presented in Figure 7(a). A change in the catalytic performance of the catalysts was noted with the variation of the Si/Al molar ratio. An initial increase in glycerol conversion was observed after the addition of Al to the support. A maximum conversion of 40% was reached with the Cu/SBA-15 SiAl 15 catalyst after 5 h of reaction, ~10% higher compared to the Cu/SBA-15 catalyst. Subsequently, higher Al loadings in the support led to a decrease in the conversion, obtaining the lowest activity of 12% with the sample with the highest Al content (Cu/SBA-15 SiAl 2) at 5 h of reaction.

Additionally, the specific initial reaction rate (r^0_{glyc}) was determined to rationalize these results using the glycerol conversion data during the first 120 minutes of the reaction. Table 6 summarizes the catalytic activity of the catalysts in terms of the specific initial reaction rate of glycerol consumption (r^0_{glyc}) expressed in mols of glycerol converted per mass of catalyst per unit of time. Indeed, the Cu/SBA-15 SiAl 15 catalyst presented the higher specific initial rate, with a value of 6.3×10^{-3} $mol_{glycerol} \cdot g_{cat}^{-1} \cdot min^{-1}$. Then, a decay in the r^0_{glyc} is noted with the decrease in the Si/Al molar ratio. The Cu/SBA-15 SiAl 2 catalyst showed a r^0_{glyc} value of 1.7×10^{-3} $mol_{glycerol} \cdot g_{cat}^{-1} \cdot min^{-1}$ because of the high aluminum loading. This means that this kinetic parameter increases with a low aluminum load in the sample.

The highest specific initial rate of Cu/SBA-15 SiAl 15 catalyst could be explained by at least two complementary effects. The first effect would be related to the acidity of the material, in which the amount of acid sites increased as a result of the interaction of the Cu species with the adjacent Al^{3+} sites. The second effect would be related to the nature of the Cu phase which in turn encompasses three aspects: (i) the first aspect is the interaction between the Cu species with the intra-network Al species incorporated in the support, which was as seen reflected in the decrease in the reducibility of the Cu phase with the increase in the Al loading observed both in the H_2-TPR tests and in the passivation by N_2O-TPR. (ii) The second aspect refers to the availability of active copper surface, which decreases with increasing Al loading, as determined by the N_2O-TPR passivation method. (iii) The third aspect refers to the presence of mononuclear $Cu^{\delta+}$ species, which is related to the geometry and coordination of the copper species observed by UV-Vis DRS.

The product distribution profiles and the yield towards HA and 1,2-PDO were compared as a function of the reaction time of the series of catalysts (Figure 7(b)–(e)). In general terms, HA was the main product of

the reaction for all catalysts, with selectivity values greater than 80% during the first minutes of the reaction. Likewise, the compounds that were identified in high proportions were 1,2-PDO and pyruvaldehyde, while another set of products such as acetone, propionaldehyde, ethylene glycol, 1,4-dioxane, as well as groups of alcohols (methanol, 1-propanol, 2-propanol) and acids (propionic acid and acrylic acid) were detected in lower proportions. Finally, a series of compounds grouped into ¨Others¨ were observed in the reaction mixture but not identified and whose selectivity increases at high reaction times.

The Cu/SBA-15 SiAl 2 catalyst presents marked differences in the products selectivity. At short reaction times (< 90 minutes) a noticeable selectivity towards pyruvaldehyde was observed. Subsequently, as the reaction time proceeds, longer reaction times (> 90 minutes) result in greater selectivity towards HA and 1,2-PDO.

Here it is relevant to emphasize the reaction mechanisms proposed in the literature. Two mechanisms have been proposed in the transformation of glycerol to 1,2-PDO (Scheme 2)**[12, 124]**. The first involves a dehydration-hydrogenation mechanism, where glycerol is dehydrated to HA and subsequently hydrogenated to 1,2-PDO. It is accepted that dehydration proceeds in the acidic sites of the support, while the metal promotes the hydrogenation step. In the second mechanism (dehydrogenation-dehydration-hydrogenation) glycerol dehydrogenate to glyceraldehyde which is then dehydrated to 2-hydroxyacrolein and its isomer pyruvaldehyde. Then 1,2-PDO is formed by the hydrogenation of the pyruvaldehyde. On the other hand, direct hydrogenolysis of glycerol is also possible, which leads to the formation of ethylene glycol through the cleavage of a C–C bond in a hydrogenation step. However, this route is usually not favored in Cu-based catalysts due to its intrinsic ability to selectively break C–O bonds without breaking C–C bonds**[125]**.

That said, the selectivity profile indicates that the presence of high amounts of Al (Si/Al = 2) favors the glycerol dehydrogenation pathway during the first minutes of the reaction and longer times favor the dehydration-hydrogenation pathway. This behavior can be explained by two factors present in this catalyst: (1) the presence of larger copper domains on the surface facilitates access for glycerol molecules (ensemble size), favoring the formation of hydrogen *in-situ* and glyceraldehyde by dehydrogenation of glycerol in the first minutes of the reaction, due to the inert condition of N_2 atmosphere. (2) Due to the presence of more acid sites, glycerol molecules have a high chance to adsorb on the acid centers and follow a dehydrogenation pathway generating HA as an intermediate species**[126]**. Additionally, a slight increase in selectivity to ethylene glycol and alcohols was observed. Thus, the hydrogenolysis route also occurs.

In contrast, the highly dispersed copper with smaller domain sizes located inside the SBA-15 matrix (Si/Al > 2 molar ratios) does not seem to be able to facilitate the dehydrogenation of glycerol and the hydrogenation of HA to promote the formation of glyceraldehyde and 1,2-PDO, respectively.

These results suggest that the interaction between the active copper phase and the aluminum-modified supports affects the stability of the copper species leading to differences in glycerol transformation pathways.

Figure 7(f) shows the distribution of products and the yield towards HA and 1,2-PDO for the Cu/SBA-15 and Cu/SBA-15 SiAl catalysts at 90 minutes of reaction. A very slight decrease in the selectivity towards HA was evidenced with the progressive increase in the Al content, remaining around ~80% for the ratios Si/Al = ∞, 15 and 10 (84, 84, and 81% respectively). Nevertheless, this decrease becomes much more evident in the material with the highest Al load (~50% selectivity). At the same time, an increase in selectivity towards 1,2-PDO was witnessed, indicating that the addition of high amounts of Al promotes the breaking of C–O bonds.

Given that at Si/Al ≥ 10 molar ratios the selectivity towards HA remains practically constant, it can be inferred that in these catalysts, the dehydration of glycerol is initially preferred over the other parallel and consecutive reactions that may involve the catalytic process. While at a Si/Al = 2 molar ratio, other reaction routes are favored that lead to the formation of other products. Selectivity towards 1,2-PDO and pyruvaldehyde is favored with this Si/Al ratio. This suggests that the Cu/SBA-15 Si/Al 2 catalyst favors a pathway involving a glycerol C–O bond cleavage step followed by a hydrogenation step.

In Figures 7(g) and Figure 7(h), the curves expressing the quantity of formation of HA and 1,2-PDO for the series of catalysts are presented. The values of the specific initial reaction rate of the formation of HA and 1,2-PDO are presented in Table 6.

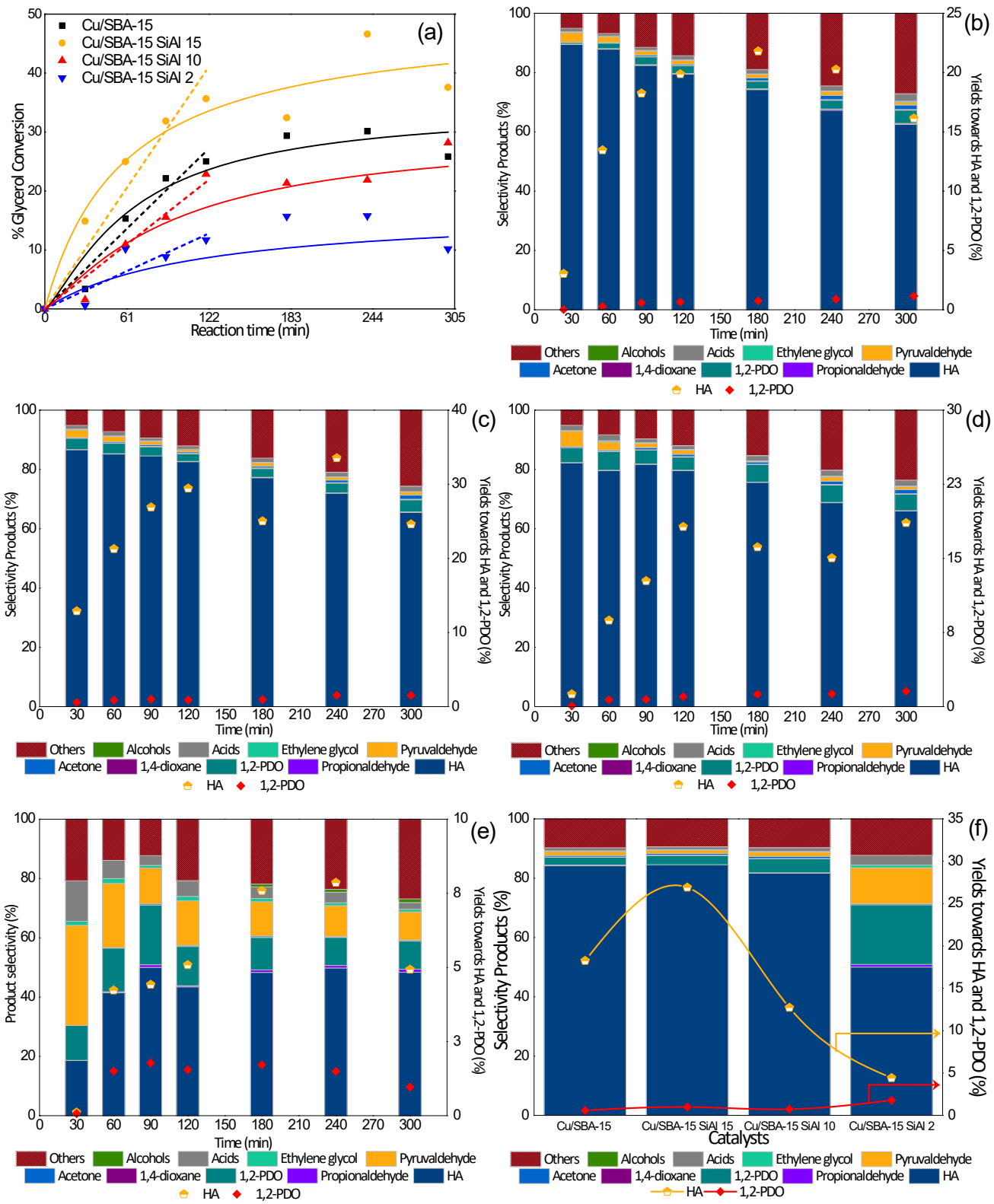
(a)
Cu/SBA-15
Cu/SBA-15 SiAl 15
Cu/SBA-15 SiAl 10
Cu/SBA-15 SiAl 2
% Glycerol Conversion
Reaction time (min)
(b)
Selectivity Products (%)
Yields towards HA and 1,2-PDO (%)
Time (min)
(c)
(d)
(e)
Product selectivity (%)
(f)
Selectivity Products (%)
Yields towards HA and 1,2-PDO (%)
Catalysts
Cu/SBA-15
Cu/SBA-15 SiAl 15
Cu/SBA-15 SiAl 10
Cu/SBA-15 SiAl 2
Others
Alcohols
Acids
Ethylene glycol
Pyruvaldehyde
Acetone
1,4-dioxane
1,2-PDO
Propionaldehyde
HA

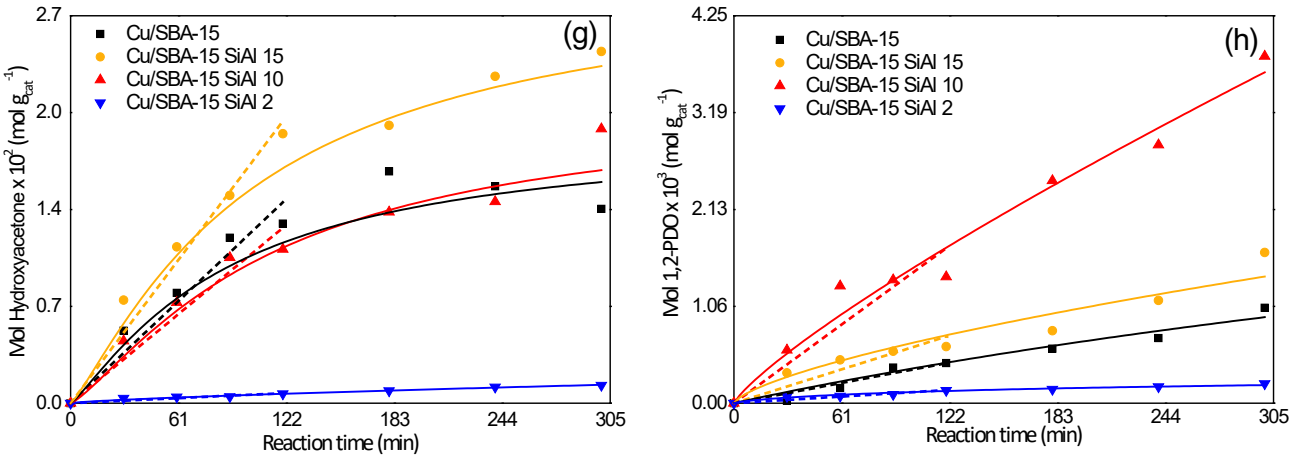

Figure 7. (a) Glycerol conversion curves as a function of time. Specific rate calculations with conversion data up to 120 min of reaction. Product selectivity and yield towards HA and 1,2-PDO as a function of reaction time for catalysts: (b) Cu/SBA-15, (c) Cu/SBA-15 SiAl 15, (d) Cu/SBA-15 SiAl 10, (e) Cu/SBA-15 SiAl 2. (f) Product distribution and yield to hydroxyacetone obtained at 90 min of reaction for the catalyst series. Profiles of quantity of formation of (g) Hydroxyacetone and (h) 1,2-PDO.

Table 6. Specific initial reaction rate of glycerol consumption (r^0_{glyc}) after 120 minutes of reaction. Initial reaction rate of formation of HA (r^0_{HA}) and 1,2-PDO ($r^0_{1,2-PDO}$).

Sample	$r^0_{glyc} \times 10^{-3}$ ($mol_{glycerol}\ g_{cat}^{-1} \cdot min^{-1}$)	$r^0_{HA} \times 10^{-4}$ ($mol_{HA}\ g_{cat}^{-1} \cdot min^{-1}$)	$r^0_{1,2-PDO} \times 10^{-5}$ ($mol_{1,2\text{-}PDO} \cdot g_{cat}^{-1}\ min^{-1}$)
Cu/SBA-15	3.7	3.88	1.21
Cu/SBA-15 SiAl	6.3	5.35	1.99
Cu/SBA-15 SiAl	3.1	3.36	4.68
Cu/SBA-15 SiAl 2	1.7	0.19	0.39

Considering the reaction pathways described before, it is then inferred that copper can serve as an active site for the dehydrogenation/hydrogenation steps as shown in Scheme 2. This gives rise to active hydrogen atoms that can participate during the catalytic process given that the reaction conditions are carried out in an N_2 environment without external H_2 supply. This could explain the origin of the formation of pyruvaldehyde and 1,2-propanediol. To this point, it is important to report that Yfanti et al.**[124]** attributed the formation of H_2 *in-situ* by reforming in aqueous phase of methanol to the hydrodeoxygenation (HDO) of glycerol. They observed that when a 9% v/v aqueous solution of glycerol is used as feed in the absence of methanol, the glycerol was converted by almost 88% and 1,2-PDO was identified with a selectivity of 30.4%. Recently, Gallego et al.**[127]** have investigated the formation of H_2 *in-situ* in the hydrogenolysis of

glycerol with Nb-doped nickel-based catalysts. They indicate that the rate of H_2 formation *in-situ* can match the hydrogen demand required for optimal 1,2-PDO production, being more advantageous, rather than external H_2 feeding, which leads to the formation of over-hydrogenation products. These results imply that when glycerol and water are used as feed, a part of the glycerol is consumed, forming hydrogen, and another part remains available for HDO reactions. From this, it is concluded that a proper balance between the hydrogenation-dehydrogenation and dehydration centers are crucial to achieve better selectivity towards 1,2-PDO.

Although the degradation of the texture and structure of the materials also has an influence on the catalytic performance of these systems, other factors may also have relevance to explain the differences in the observed catalytic activity behavior, such as the material acidity and the availability of Cu active sites on the surface.

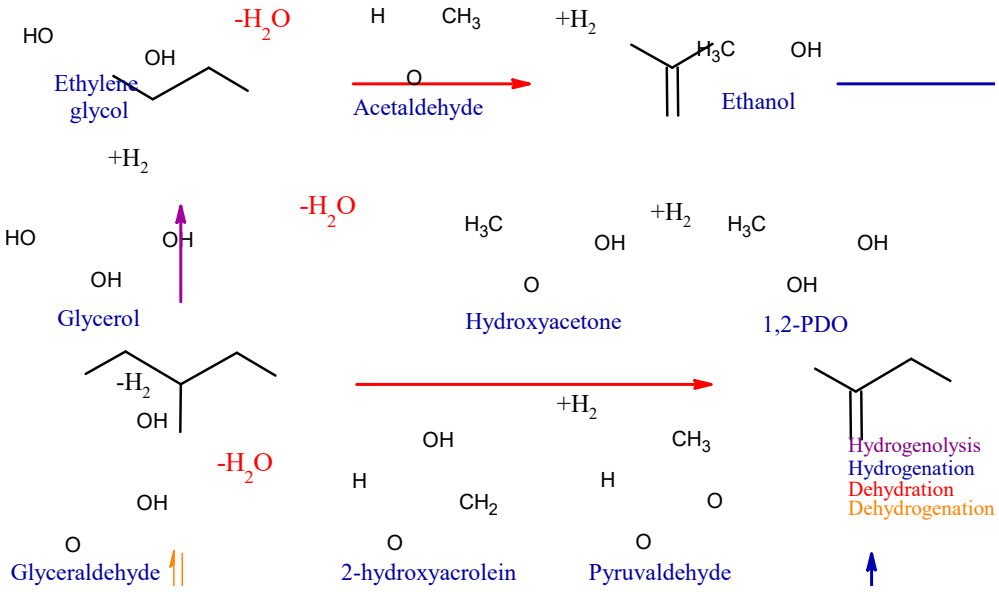

Scheme 2. Possible reaction pathways of glycerol**[125]**.

It was found that the sample with molar ratio Si/Al = 15 achieved the highest glycerol conversion and that the decrease in the Si/Al ratio resulted in a drop in conversion and selectivity. Thus, acid sites can promote the formation of secondary products. This is mirrored in an increase in the distribution of products, as well as a greater acidity can lead to the formation of carbon deposits on the catalytic surface, disabling the active sites on the surface during the first-time intervals of the reaction, which consequently implies a decrease in the conversion (See section 3.3). However, acidity alone is not enough parameter to explain the catalytic behavior of these materials in the reaction. The role of the copper phase in the catalytic performance must

also be considered. Changes in catalytic behavior must also be covered from the point of view of the role played by copper species in the transformation of glycerol. Copper species are relevant due to their dehydrating and hydrogenating/dehydrogenating capacity in the conversion of glycerol**[124]**. From the results of TPR of the catalysts previously passivated by N_2O (Figure 3(b)), it can be inferred that the introduction of Al in SBA-15 can stabilize the Cu particles through a metal-support interaction. In addition, the incorporation of Al into the framework of mesoporous silica induces the creation of structural defects, which can act as anchoring sites to immobilize the copper particles that are deposited in these domains**[85]**.

Tentatively, it is possible to state that the introduction of a molar ratio (Si/Al = 15) could favor an optimal interaction because the incorporation of Al species in the mesoporous silica network could generate structural defects. The FTIR spectra in the OH region after thermal treatment at 150 °C in Ar flow (Figure 4(b)) indicated a distortion of nests of silanol groups of SBA-15 with the introduction of Al species, which would generate structural defects. These defects would act as anchoring sites for copper species through generated vacancies, which would allow not only the stability of the copper particles and prevention of their sintering but also the promotion of a better electronic transfer between the active copper species and support. In this context, it is important to highlight that the Cu/SBA-15 SiAl 15 catalyst presented a majority fraction of copper species distributed in a dispersed manner along with the appearance of a minority fraction of oligomeric species, as evidenced by the UV-Vis DRS technique (Figure 5). This would indicate stability promoted by the strong anchoring of the copper species with the support, particularly for the copper species with interaction in adjacent domains with the intra-lattice aluminum species. Likewise, ^{27}Al-MAS-NMR (Figure S5) demonstrated the exclusive presence of Al-tetrahedral species incorporated in the support of the Cu/SBA-15 SiAl 15 catalyst. It is also conceivable that the XRD analysis (Figure 8(d)) of this post-reaction material revealed weak diffractions of copper phases, indicating stability against sintering. The deposition of carbonaceous species in the post-reaction material was also dependent on the Al loading. These results demonstrate that the variation of Si/Al molar ratio has a remarkable effect on the performance of the Cu/Al-SBA-15 catalysts.

3.3. Characterization of post-reaction catalysts

After the catalytic tests, the solids were recovered by centrifugation from the reaction mixture, washed with deionized water, dried, and characterized to obtain more information on their properties and to correlate the changes in their properties with the catalytic performance.

The copper chemical composition of the materials recovered after the first test (post-reaction) measured by ICP-MS is summarized in Table S1. The results of these analyses revealed a loss of copper species in the post-reaction materials suggesting that copper leaching is one of the factors participating in the deactivation of the catalysts. For aluminosilicate materials in acidic medium, it is common for a hydrolysis of the Si-O-Al bonds to occur. These generate extra-network Al species which give rise to octahedral Al species that end up suffering leaching more easily than intra-network Al species**[128]**.

The N_2 physisorption isotherms and pore size distribution curves of the post-reaction samples are presented respectively in Figure 8(a) and (b). As can be seen, the analyses do not reveal a marked difference in the shape of the isotherms compared to the isotherms of the fresh samples, compared with Figure 1(a), showing conservation of the hysteresis loops which seems to suggest that the mesostructured character of the SBA-15 is preserved.

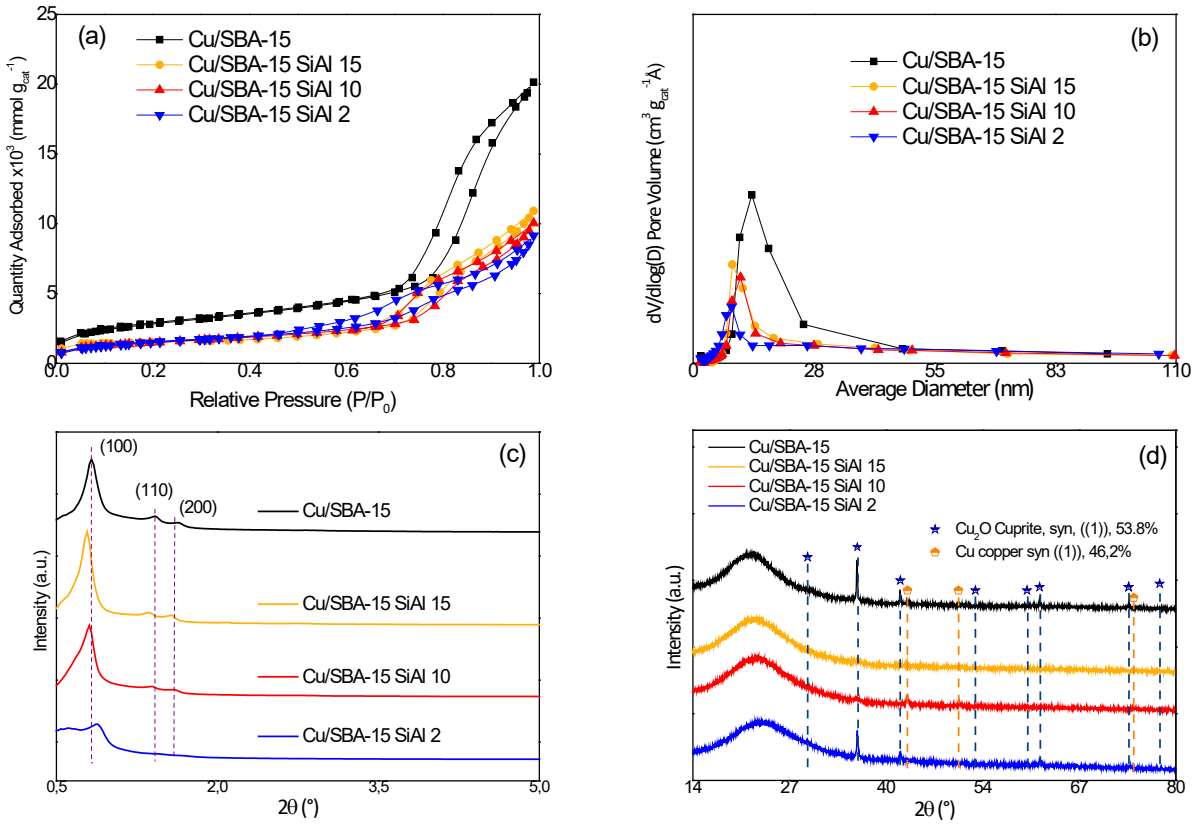

Figure 8. (a) N_2 adsorption-desorption isotherms and (b) pore size distribution of the used catalysts. XRD profiles in the range of (c) low-angles and (d) high-angles of post-reaction samples.

Figure 8(c) and Figure8(d) show the low-angle and high-angle diffraction patterns, respectively, of the post-reaction catalysts for comparison purposes. The diffraction patterns in the low-angle region indicate that the mesostructured character of SBA-15 is preserved, revealing the characteristic peaks associated with the reflections of the crystallographic planes of the hexagonal symmetry of the support. No considerable changes in the profiles are evident in relation to the fresh catalysts, except for a slight decrease in the intensity of these reflections.

Diffraction patterns at high-angles detected the presence of diffraction peaks. The diffraction peaks with angles 2θ at 29.6°, 36.4°, 42.2°, 61.4°, and 73.6° correspond to crystalline phase of cuprite (Cu_2O, PDF 05-0667) while the diffraction signals with angles 2θ at 43.4° and 50.5° correspond to metallic copper (Cu^0, PDF 04-0836). The diffraction lines of the XRD profiles of the Cu/SBA-15 and Cu/SBA-15 SiAl 2 catalysts are associated with the Cu_2O cuprite species. This indicates that during the catalytic reaction, copper species

agglomerate and undergo oxidation, decreasing the catalytic performance, especially for the Cu/SBA-15 and Cu/SBA-15 SiAl 2 catalysts. On the other hand, the XRD profiles of the Cu/SBA-15 Si/Al 15 and Cu/SBA-15 Si/Al 10 catalysts exhibit weak diffractions characteristic of Cu^0. The possible presence of metallic Cu and the absence of high intensity peaks in these samples suggest that under these Si/Al molar ratios the phase of copper is more stabilized, reaching a lower energy configuration, and maintaining dispersion. It should also be noted that the diffraction peaks attributed to Al_2O_3 were not identified.

It is important to emphasize that through XRD analysis of the post-reaction catalysts (Figure 8(c) and Figure8(d)), no notable peak accounting for carbonaceous species was observed, which indicates its amorphous nature. In addition, aluminum species can stabilize the Cu particles deposited on the support. This stabilization is attributed to the structural defects induced by the incorporation of Al in the SBA-15 structure. Nevertheless, the formation of Al species segregated to the outside of the SBA-15 structure can result in the segregation of Cu species**[85]**. The copper sintering is more inhibited in the Cu/SBA-15 SiAl 15 and Cu/SBA-15 SiAl 10 samples.

The data provided in Table S2 demonstrate a change in the textural parameters of the post-reaction samples. A decrease in the specific surface area was noted compared with the fresh samples (Table 2), which can be attributed to the presence of carbonaceous deposits on the surface once the samples were washed, dried, but not calcined. This decrease seems to be less pronounced in the Cu/SBA-15 material compared to the rest of the samples containing aluminum. Taking into consideration that the insertion of Al in SBA-15 contributes to the modification of the acidic properties of the system, it is reasonable to expect that an increase in the concentration of surface acid sites can promote deactivation processes due to the formation of carbonaceous deposits on the catalytic surface. This was mirrored in a pronounced decrease in the specific surface area of the materials containing aluminum. The same reasoning can explain the decrease in the average pore volume, where carbonaceous deposits can block part of the mesoporous network of the material. On the other hand, the average pore diameter presented an increase in its values which were more considerable in the samples containing aluminum (7.3 - 8.5 nm (Table 2) to 8.6 - 12.6 nm (Table S2) for the fresh and used samples, respectively) compared to the sample containing only Si (11.4 (Table 2) to 11.6 nm (Table S2) for the fresh and used sample respectively). This can be tentatively attributed to pore melting because of a partial collapse of the porous mesostructure of the material.

Temperature-programmed oxidation (TPO) analyses have indicated the presence of carbonaceous species accumulated on the surface during the reaction. The formation of carbon deposits reduces the number of

active sites available on the surface, compromising the catalytic performance. Through the TPO analysis (Figure S6), the Cu/SBA-15 SiAl 15 catalyst presented a lower content of deposited carbonaceous species, in relation to the other catalysts containing Al. In addition, the Cu/(Si+Al) surface atomic ratio (Table 5) suggested a higher fraction of copper atoms exposed on the surface of this catalyst compared to other aluminum-containing materials. These factors suggest an optimal interaction between the copper and aluminum species for the Cu/SBA-15 SiAl 15 catalyst. However, an excessive load of aluminum species could result in a stronger interaction with the Cu species, compromising the reducibility of copper, affecting the metal component, and inducing a decrease in the active copper surface.

Figure S6 shows the TPO profiles and Table 7 summarizes the quantification of the total amount of NH_3 desorbed from the fresh catalysts along with the O_2 consumption by TPO of the post-reaction catalysts in the temperature range between 45-850 °C. A desorption signal is observed in all catalysts within this temperature range, revealing the formation of carbonaceous deposits during the reaction. The signal slightly increases in intensity and becomes broader as the Al loading in the samples increases, revealing the formation of carbonaceous deposits during the reaction (Figure S6). The carbon content must be related to the amount of acid sites available on the surface. This trend is consistent with differences in catalytic activity, where the increase in the proportion and strength of acid sites favors the dehydration of glycerol as well as the generation of secondary products particularly for the Cu/SBA-15 SiAl 2 catalyst. The acidity of the catalyst plays an important role not only in its activity and selectivity in the dehydration of glycerol, but also in its stability or resistance to deactivation. To substantiate the greatest deposition of carbonaceous species on the Cu/SBA-15 SiAl 2 catalyst is important to emphasize that this material presented the greatest amount of Brönsted (20 $\mu mol \cdot g^{-1}$) and Lewis (121 $\mu mol \cdot g^{-1}$) acid centers, as expressed by the FTIR spectroscopy data of pyridine adsorption in Table 3. Very strong acid sites, mainly Brönsted acid sites, would promote the formation of carbonaceous species inducing the deactivation of the catalyst by pore blocking**[129]**.

Table 7. Quantification of NH_3 of the fresh material and TPO of the used material.

Sample	NH_3-TPD ($\mu mol \cdot g^{-1}$)	TPO ($\mu mol \cdot g^{-1}$)
Cu/SBA-15	990	51
Cu/SBA-15 SiAl 15	772	65
Cu/SBA-15 SiAl 10	764	76
Cu/SBA-15 SiAl 2	1629	113

Additionally, FTIR transmission spectra of the catalysts were used to evaluate changes in the structure of the samples after the reaction (Figure S7). In general terms, the structural integrity of the samples was maintained, indicating that it was not affected. It is well known that mesoporous materials of the SBA-15 type exhibit high hydrothermal stability, which is associated with the wall thickness**[33]**. Additionally, the incorporation of metal heteroatoms also contributes to better stability of the material, which can be attributed to the formation of a protective layer due to the deposition of these species on the surface of the mesoporous channels**[46]**. It is worth noting that a weakening is seen in the intensity of the bands corresponding to the vibrational modes of stretching the (ν) T–O bond (958 cm^{-1}) and bending of the (δ) Si–O–T bond (T = Si o Al) (806 cm^{-1}), in the materials Cu/SBA-15 SiAl 10 and Cu/SBA-15 SiAl 2 in relation to the fresh ones. This can possibly be attributed to a redistribution of the heteroatoms in the structure, maybe forming small clusters as suggested by the XRD results, which could also explain the decrease in catalytic activity obtained with these catalysts.

From these characterization results of the post-reaction catalysts, it is possible to conclude that the structural characteristics of SBA-15 in the materials are not strongly affected. However, the diffraction profiles in the high-angle range reveal the sintering of copper species due to the appearance of copper oxide (I) and metallic copper phases. Sintering of the copper particles during the catalytic test may be one of the factors contributing to the deactivation and the observed catalytic activity trend. In fact, the detection of only the metallic copper phase in the Cu/SBA-15 SiAl 15 and Cu/SBA-15 SiAl 10 catalysts indicates that the metallic copper species remain more stabilized in these samples. On the other hand, for the Cu/SBA-15 and Cu/SBA-15 SiAl 2 catalysts it is noted that the copper species suffer sintering and partial oxidation, forming Cu_2O species that are even observed by XRD. A possible reason for the stability of the copper phase presented in the Cu/SBA-15 SiAl 15 and Cu/SBA-15 SiAl 10 catalysts can be due to the interaction with the aluminum species as suggested by the results of H_2-TPR (Figure 3(a)). The structural defects (oxygen vacancy) of the support induced by the introduction of Al in the appropriate amount can act as anchoring sites, then reducing

the mobility of the Cu particles, thus providing a greater number of active metal centers on the surface**[85]**. Then, in the case of the Cu/SBA-15 SiAl 2 catalyst, the highest Al loading fails to inhibit the segregation of the copper species, which reduces the number of sites of active Cu, decreasing their contribution to the catalytic performance of the reaction.

The TPO results indicated that the carbonaceous species amount accumulated on the catalytic surface is directly related to the evolution in the acidity of the materials due to the variation of the Si/Al ratio. Therefore, it could be concluded that the gradual decrease in glycerol conversion with Si/Al < 15 molar ratios is caused by the loss of active sites due to the accumulation of carbon species in these positions. This occurs especially to a greater extent with the sample with the highest Al load, where the greater availability of acid centers favors other glycerol transformation pathways that lead to decomposed products.

3.4 Recycling

To study the recycle ability and the deactivation behavior of the most active catalyst Cu/SBA-15 SiAl 15 we carry out the recycle experiments. The procedure is detailed in the Supplementary Material.
Table 8 presents the results of the ICP-MS analyses of the catalyst recovered after the 3rd cycle. These results reveal a notable loss of copper charge after consecutive catalytic tests.

Table 8. Copper content (%wt.), textural and structural properties of the Cu/SBA-15 SiAl 15 fresh, post 1st cycle, and post 3rd cycle.

Sample	Cu (% wt.)	S_{BET} ($m^2 \cdot g^{-1}$)	V_P[a] ($cm^3 \cdot g^{-1}$)	d_p[b] (nm)	d_{100}[c] (nm)	a_0[d] (nm)	w[e] (nm)
Cu/SBA-15 SiAl 15 fresh	5.0	208	0.44	8.5	11.4	13.2	4.7
Cu/SBA-15 SiAl 15 1st cycle	n.d.	103	0.33	12.6	11.4	13.2	4.7
Cu/SBA-15 SiAl 15 3rd cycle	0.3	2	0.00	2.2	n.d.	n.d.	n.d.
Cu/SBA-15 SiAl 15 3rd catalytic cycle regenerated	n.d.	182	0.38	8.4	11.1	12.8	4.4

[a] Pore volume calculated at P/P_0 = 0.95. [b] BJH desorption average pore diameter. [c] Interplanar distance of (100) reflection. [d] Unit cell parameter: $\left(a_0 = 2 \times \frac{d_{100}}{\sqrt{3}}\right)$. [e] Pore wall thickness: $w = a_0 - d_p$.

n.d.: not determined.

Figure 9(a) shows the comparison of the results of glycerol conversion in the reusability study between the first and the third catalytic test. Glycerol conversion decreased from 42% to 6.4%. Figure 9(b) presents the product selectivity that was obtained in the third test. At the first 90 minutes of the reaction, it is observed that the selectivity towards HA ranges between 53-65% and the selectivity towards pyruvaldehyde is around 12%. Then, at longer reaction times, the selectivity towards HA increases reaching values between 67-85% while the selectivity towards pyruvaldehyde decreases between 7-0%. Regarding the yield towards HA and 1,2-PDO, after 180 minutes of reaction with values of 5.7 and 0.5% respectively. The product distribution profiles and the yields towards HA and 1,2-PDO between the first and third cycles calculated after 90 minutes of reaction are shown in Figure 9(c). It can be observed that after the third test, the selectivity towards pyruvaldehyde and other products increases while the selectivity towards HA decreases from 84% to 61%. An increase in the formation of compounds that were not identified and denoted as "Others" is also observed. Likewise, the selectivity of HA and 1,2-PDO decreased drastically in the third reuse. Considering the ICP-MS results given in Table 8, this drop in the conversion and the increase in selectivity towards

pyruvaldehyde and other unidentified compounds indicates that there is a close relationship between the catalytic performance with the availability of the copper phase in the catalytic system. The loss in the number of copper sites by leaching compromises the catalytic performance. At this condition, glycerol reacts via dehydration to form HA as an intermediate species and then this intermediate is dehydrogenated towards pyruvaldehyde in the few available copper metal centers.

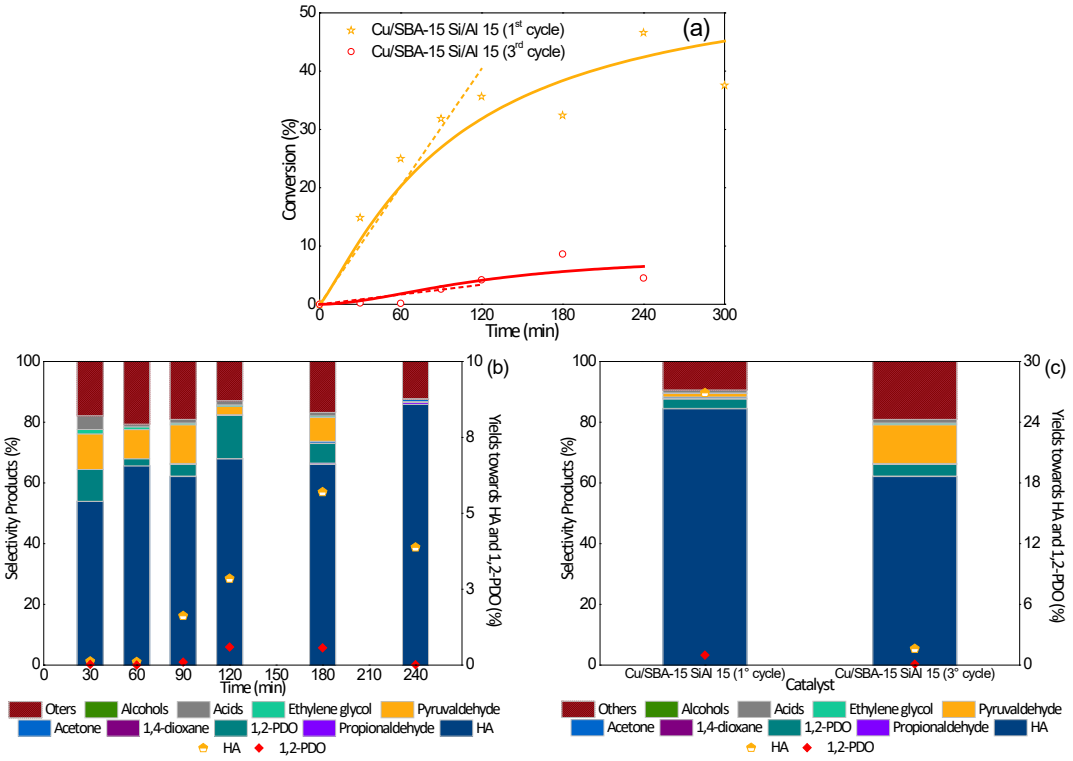

Figure 9. Reusability of the Cu/SBA-15 SiAl 15 catalyst. (a) Comparison in the glycerol conversion between the 1st and 3rd catalytic cycle. (b) Selectivity and performance profile towards HA and 1,2-PDO as a function of the reaction time obtained in the 3rd catalytic cycle. (c) Comparison of the distribution of products and yield towards HA and 1,2-PDO calculated after 90 minutes of reaction between the 1st and 3rd cycle with the Cu/SBA-15 SiAl 15 catalyst.

The spent material recovered at the end of the third cycle was characterized by physisorption, XRD and FTIR. For comparative purposes, the properties of this material recovered after the 3rd cycle were compared with the fresh original catalyst and with the spent catalyst recovered after the 1st cycle. The characterization of this group of materials by the aforementioned techniques are presented in Figure 10. Table 8 also summarizes the structural and textural properties of these samples. Figure 10(a) and (b) shows the N_2 adsorption-desorption isotherms and pore size distribution of the fresh and spent Cu/SBA-15 SiAl 15 catalyst from the 1st cycle and 3rd cycle. The change of textural properties of Cu/SBA-15 SiAl 15 material

was noticeable after the first catalytic test since a decrease in both, specific surface area and pore volume (208 to 103 $m^2 \cdot g^{-1}$ and 0.44 to 0.33 $cm^3 \cdot g^{-1}$ respectively) and an increase in the pore diameter (8.5 to 12.6 nm). It could be consequence of the retention of the organic moieties on the surface of the catalyst. Whereas the used material of the 3rd cycle was not able to adsorb N_2. Once this last material is regenerated by a calcination step, it seems to recover part of the original textural properties of the fresh material. These differences observed between the spent materials and the material that was regenerated from the calcination stage seems to suggest that there exists the formation of carbonaceous deposits on the surface that are released during the calcination stage. This could be supported by the FTIR results shown below.

Structural compromise is observed in the organization of the SBA-15 after the third reaction cycle since the characteristic reflections to the hexagonal symmetry planes of the SBA-15 system were hardly detected in the region of the low-angle interval (Figure 10(c)). Meanwhile, in the high-angle range (Figure 10(d)), it was observed that after the 1st cycle, the copper phase undergoes a slight agglomeration due to the presence of a weak signal corresponding to Cu^0. On the other hand, in the material recovered after the 3rd cycle, no diffraction signals corresponding to copper or alumina phases were identified, only the presence of the broad diffraction peak corresponding to amorphous silica was observed. This result, complemented by the ICP-MS results, suggests that Cu undergoes re-dispersion, possibly due to the calcination and reduction activation processes that induce the mobility of the copper particles, losing the interaction with the support, and being more susceptible to leaching. Figure 10(e) shows, for comparison purposes, the FTIR spectra in the 360-4000 cm^{-1} region of the Cu/SBA-15 SiAl 15 catalyst recovered from the 1st and 3rd cycle, and additionally of the material recovered from the 3rd cycle that was regenerated by calcination. In the spectrum of the material recovered after the 3rd cycle, marked bands were observed at 2941 and 2882 cm^{-1} corresponding to the stretching vibration of C-H bonds of the carbon type sp^3 hybridization. The band at 1639 cm^{-1} corresponds to the stretching vibration of a C=C bond, while the bands between 1410-1460 cm^{-1} correspond to the bending vibrations of C-H bonds associated with aromatic compounds. These bands disappear after regenerating the material by a calcination step and show that the reaction follows a polycondensation and/or cyclization pathway which can be formed by the presence of a greater fraction of the active surface centers as acidic centers rather than metallic copper centers. The presence of a greater proportion of copper metal centers would help to stabilize the evolution of the reaction due to its dehydrogenating/hydrogenating capacity, ceasing condensation routes and preventing the formation of large amounts of heavy compounds and carbon deposits on the catalyst.

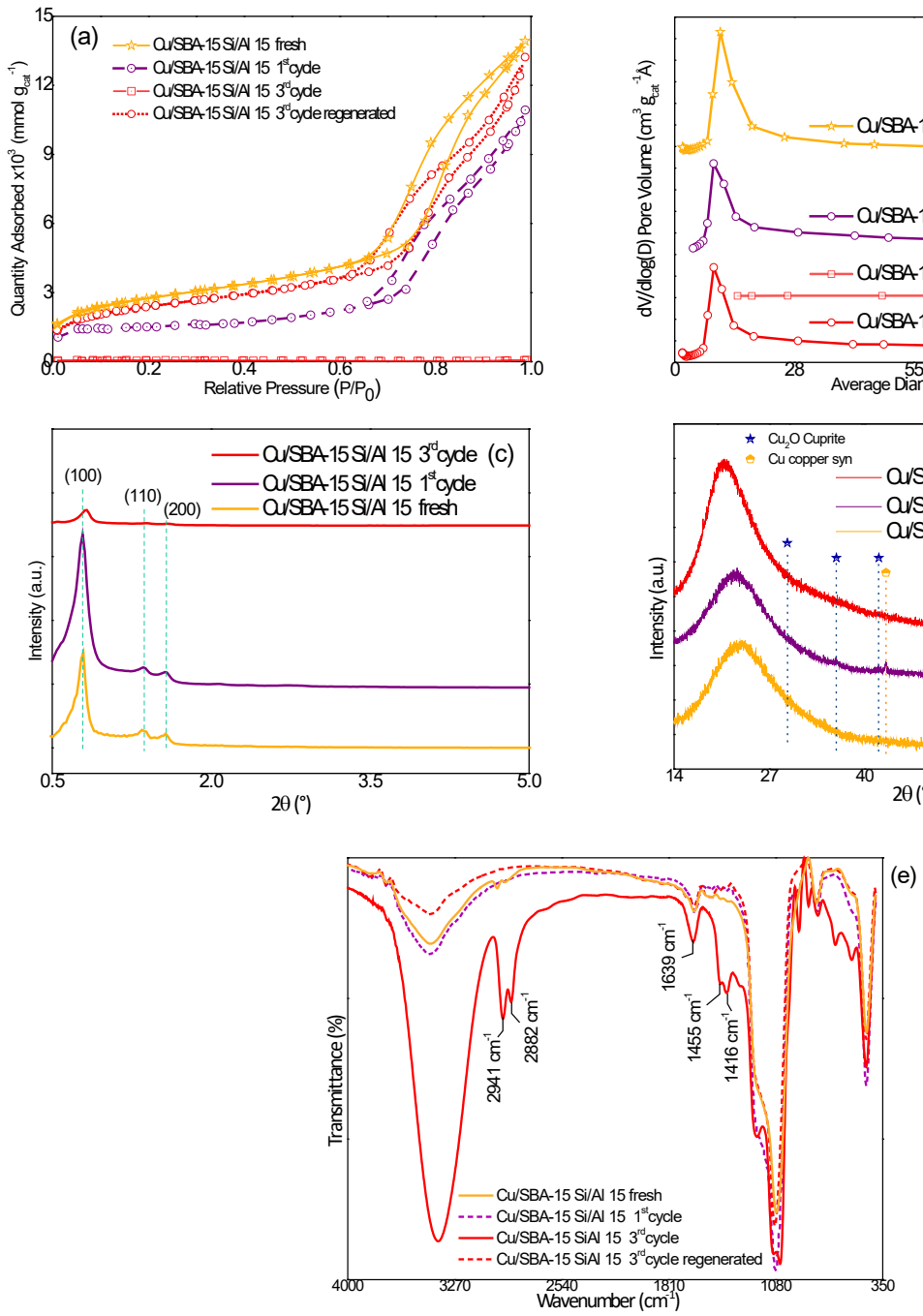

Figure 10. (a) N_2 adsorption-desorption isotherms. (b) Pore size distribution. (c) XRD profiles in the range of low-angles and (d) high-angles. (e) FTIR spectra of the material fresh and recovered from the 1st and 3rd cycle and of the material regenerated by calcination after the 3rd cycle of the Cu/SBA-15 SiAl 15 catalyst.

From these results, it can be deduced that the loss of catalytic activity observed in the catalytic tests can be attributed to the combination of two effects. (i) On the one hand, the effect of the catalyst activation treatment (*ex-situ* reduction) used after each recycling intervenes, which can weaken the interaction of the copper species with the support, making the copper phase susceptible to undergo leaching after each catalytic process. Furthermore, the reaction in the aqueous medium also affects the stability of the structure. This is corroborated by the weakening of the reflections associated with the plane's symmetry of SBA-15 observed by XRD patterns in the low-angle range. (ii) Catalytic deactivation as a consequence of the formation of carbonaceous species during the catalytic reaction that was evidenced by the FTIR spectrum of the post-3rd cycling material (Figure 10(e)).

Therefore, due to the thermal treatments applied to regenerate the catalyst, a decrease in the mobility of the copper species may occur, losing the established interaction with the support and a loss of the copper phase through leaching may easily occur in each consecutive catalytic process. This decrease implies that there is a greater proportion of acidic centers instead of metallic ones present on the surface after the reaction tests, which may lead to the conversion of glycerol being carried out through polycondensation pathways that generate secondary products and, in the end, a more severe deposition of carbonaceous species on the surface.

4. Insights into catalytic performance

According to the set of characterization and catalytic activity results, the catalysts prepared by the pH-adjusting method and the ammonia evaporation method present high-performance activity in the dehydration of glycerol towards hydroxyacetone in the absence of a reducing atmosphere. The catalytic activity exhibited by these catalysts is the result of the insertion of Al species (modification of the Si/Al molar ratio) in the SBA-15 structure that regulates different parameters of the system. The variation of the Si/Al molar ratio developed a strong influence on the regulation of acid sites, structure defects, agglomeration of Cu and Al species, reducibility of catalysts, and formation of carbon deposits during catalytic activity.

The proper quantity of Lewis acid sites corroborated the rationalization proposed with respect to the change observed in the catalytic activity, distribution of products, and deposition of post-reaction carbonaceous species. The conversion of glycerol and the selectivity towards the products were dependent on the acidity. The role of the Lewis acid sites determined by Py-FTIR spectroscopy is very clearly seen when the data on the specific initial rate of glycerol consumption (r^0_{glyc}) expressed in $mol_{glycerol} \cdot g_{cat}^{-1} \cdot min^{-1}$ are represented in a graph as a function of the amount of Lewis acid sites expressed in terms of $\mu mol \cdot g_{cat}^{-1}$ as indicated in Figure 11(a). There is a close correlation between r^0_{glyc} with the number of Lewis acid sites. A maximum in r^0_{glyc} was observed for the Cu/SBA-15 SiAl 15 catalyst. On the other hand, the effect of acidity on the r^0_{glyc} resulted in a significant inhibition, particularly for the Cu/SBA-15 SiAl 2 catalyst which presented a lower r^0_{glyc} with the value of 1.7×10^{-3} $mol_{glycerol} \cdot g_{cat}^{-1} \cdot min^{-1}$ (Table 6). Furthermore, the Cu/SBA-15 SiAl 2 catalyst presented the greatest amount of Lewis acid sites with the value of 121 $\mu mol \cdot g_{cat}^{-1}$ along with a greater amount of Brönsted acid sites with the value of 20 $\mu mol \cdot g_{cat}^{-1}$ (Table 3) compared to the other catalysts. For this catalyst, the cleavage of C–O bonds together with the hydrogenation step for the formation of pyruvaldehyde and 1,2-PDO prevailed. Likewise, other unidentified products were observed in a greater proportion. The higher availability of acidic sites led to the formation of side products in the glycerol dehydration reaction. Thus, the Lewis and Brönsted acid sites have a regulatory role in the carbonaceous species amount deposited in the catalyst which inhibits the initial rate of glycerol consumption (Figure 11(b)). Likewise, the high Al load produced a change in the textural and structural properties of the Cu/SBA-15 SiAl 2 material, which would generate the greatest accumulation of carbonaceous species, especially in the domains occupied by Cu species interacting with extra-network Al species in the outermost layers of the pores of the SBA-15. This would justify the unsaturated carbon functional groups identified by FTIR shown above in Figure 10(e).

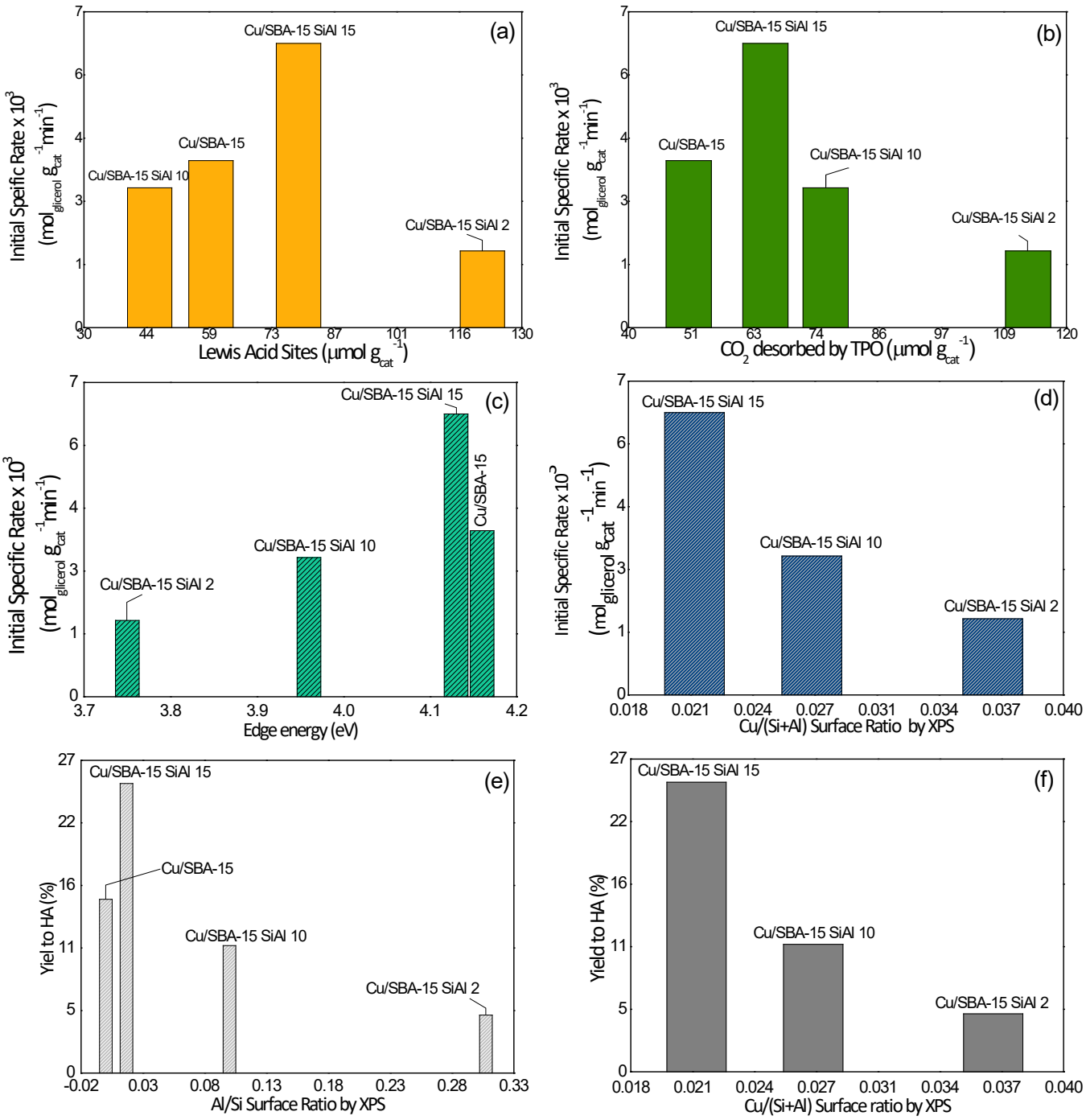

Figure 11. Dependence of the initial rate of glycerol consumption on: (a) Total amount of Lewis acid sites. (b) Total amount of carbonaceous species deposited on the post-reaction catalyst. (c) Edge energies determined by UV-Vis diffuse reflectance spectroscopy (UV-Vis DRS) and (d) surface amount of copper determined by X-ray photoelectron spectroscopy (XPS). (e) Correlation between the initial rate of glycerol consumption with Al/Si surface ratio and (f) Cu/(Si+Al) surface ratio on the catalysts determined by XPS.

All catalysts containing Al species (Cu/SBA-15 SiAl 15, Cu/SBA-15 SiAl 10, and Cu/SBA-15 SiAl 2) presented a greater amount of carbonaceous species than that detected for the Cu/SBA-15 catalyst by TPO analysis (Table 7). Deposits of carbonaceous species are formed mainly in the acidic sites of the catalyst through secondary reactions. In the case of the glycerol dehydration reaction, it has been confirmed that the carbonaceous compounds responsible for the deactivation of the catalyst are mainly formed by byproducts of polycondensation and cyclization reactions of glycerol, forming polyglycols and/or polyaromatics, depending on the conditions of reaction and the physicochemical properties of the catalyst**[42]**. It is inferred that, together with the acidic centers, copper species also play an important regulatory role in both the catalytic activity and the observed selectivity.

A correlation between the initial reaction rate and the edge energies of the catalysts determined by UV-Vis diffuse reflectance spectroscopy (UV-Vis DRS) is presented in Figure 11(c). This effect is particularly notable for the Cu/SBA-15 SiAl 15 catalyst. As indicated above, for the Cu/SBA-15 SiAl 15 catalyst the Al species were incorporated at intra-lattice localities in the SBA-15 structure, forming an anchoring and a highly dispersed state of the copper species as a result of the structural vacancies generated by the perturbation of the nests of silanol groups upon the introduction of Al species as evidenced by the FTIR-OH analysis (Figure 4(b)). Similarly, complementing the UV-Vis DRS results with the XPS results of the Cu/SBA-15 SiAl 15, Cu/SBA-15 SiAl 10, and Cu/SBA-15 SiAl 2 catalysts, the surface composition of the materials and the amount of surface copper species enhanced the initial rate of glycerol consumption as shown in Figure 11(d).

Consequently, and by reasoning similar to the above, the total amount of acid sites expressed in terms of the Al/Si surface ratio in the catalysts (Figure 11(e)) and the Cu/(Al+Si) ratio (Figure 11(f)) in the Cu/SBA-15 SiAl 15, Cu/SBA-15 SiAl 10 and Cu/SBA-15 SiAl 2 catalysts demonstrate that both the surface acidity and the surface amount of copper play a determining role in the performance observed for hydroxyacetone. The highest performance towards HA observed for the Cu/SBA-15 SiAl 15 catalyst can be directly correlated with the amount of Lewis acid sites along with a highly dispersed state of the copper species as evidenced by the UV-Vis DRS analyses. Complementary to these aspects and in particular for the Cu/SBA-15 SiAl 15 catalyst, the possible stabilization of Cu^{+} species in the structural defects would be added. These copper ions would act as an electron acceptor and provide Lewis acid centers. In this regard, a decrease in the concentration of Brönsted acid sites was evidenced with the introduction of copper species (Table 3) through the results of Py-FTIR spectroscopy. This could be due to the transformation of the Brönsted acid sites to Lewis acid sites due to the interaction of the copper species with the surface of the mesoporous

silicon support, whether or not containing aluminum species. Therefore, it is tentatively possible to propose that the dehydration of glycerol necessarily requires the presence of copper species and Lewis acid sites. However, sites constituted by Cu^{2+} species could not be directly responsible for the observed dehydration since the catalyst in its initial calcined condition did not present activity as confirmed by the experimental results obtained in the present work. Other descriptors such as textural, structural, acidity, and surface properties of the copper-based catalysts must also be considered as discussed above.

5. Conclusions

Cu/Al-SBA-15 mesoporous catalysts have been found highly selective to the formation of HA for the catalytic dehydration in the liquid phase of glycerol at high concentration and in an inert N_2 atmosphere. Al was incorporated during the synthesis of the SBA-15 support by the pH-adjustment method, while Cu was introduced by the ammonia evaporation method. The results show that the Si/Al molar ratio of the supports has a significant impact on the properties and catalytic performance of the catalysts.

The incorporation of Al species in the structure of mesoporous silica SBA-15 generated changes in the textural, structural, acidity, and surface properties of the copper-based catalysts. A change in the morphology and deterioration in both uniformity and long-range structural organization of SBA-15 was observed with increasing the amount of Al in the material. Furthermore, the acidic properties were modified by the Al loading, affecting glycerol conversion and product distribution.

Moreover, it was found that the coordination environment of the Al species intervened in the anchoring of the copper species in the material, by creating structural defects as suggested by the distortion of the silanol nests observed with the incorporation of Al in the material. The interaction of Cu species with Al species produced a decrease in the reducibility of the copper phase according to the measurements by H_2-TPR and passivation by N_2O coupled to TPR. In turn, the presence of mononuclear and oligonuclear $Cu^{\delta+}$ conglomerates species, which is related to their coordination environment and their position in the mesoporous network, was dependent on the variation of the Si/Al molar ratio.

Catalytic tests showed that hydroxyacetone (HA) was the main product in the catalytic dehydration of glycerol over Cu/SBA-15 and Cu/SBA-15 SiAl catalysts. Other products such as 1,2-PDO and pyruvaldehyde were also obtained in high proportions. The higher catalytic activity and the higher yield towards HA observed on the Cu/SBA-15 SiAl 15 catalyst were attributed to a braided interlinking of the copper catalyst properties such as acidity, stability, and interaction effects between Cu species with intra-network Al species and the size domains of Cu species. These factors resulted in the prominent catalytic performance which is explained as follows: i) that there is no excess in the concentration of acid sites that end up driving the reaction through oligomerization/condensation pathways with the formation of carbon deposits and ii) the structural defects generated by the intra-network Al species isomorphically introduced into the SBA-15 matrix that promotes an electronic transfer effect from the metal to the support and greater stability of the copper species, which are present in the form of small domains.

However, an excessive concentration of Al loading decreased the catalytic activity and the distribution of products due to the formation of carbon deposits and the high availability of acid sites that promoted the formation of byproducts through secondary reactions. The formation of oligonuclear copper conglomerates was more favored due to the high aluminum loading induced a distortion of the SBA-15 silanol network while preserving the mesoporous structure along with the introduction of acidity. In addition, the Cu/SBA-15 SiAl 2 catalyst led to improved selectivity toward 1,2-PDO. This distinctive behavior, which was observed in the absence of externally added hydrogen, can be ascribed to the size of the copper species domains available to dehydrogenate glycerol to form H_2 *in-situ* in conjunction with the high amount of surface acid sites that promote the dehydration of glycerol to HA.

The stability of the Cu/SBA-15 SiAl 15 catalyst was evaluated in a series of 3 cycles. The characterization results of the catalyst after the third test suggest that the loss of catalytic activity was a result of the deposition of carbonaceous species, the structural changes of the material and leaching of the copper phase.

Acknowledgments

RJC, JCZ, and JG gratefully acknowledge the financial support from the Chilean National Fund for Science and Technology, Fondecyt N° 1180243 and N° 1220355. AFP acknowledges FCT/MCTES for financial support by national funds through the project UIDB/5006/2020. JG is grateful to the Universidad de Concepción for its cooperation with the UdeC Postgraduate Scholarship. JCZ thanks the Doctoral Scholarship N° 21201413 awarded by ANID. JL is a Serra Hunter Fellow and is grateful to ICREA Academia program and projects RTI2018-093996-B-C31 and 2017SGR128.

References

[1] H. Wang, H. Li, C.K. Lee, N.S. Mat Nanyan, G.S. Tay, A systematic review on utilization of biodiesel-derived crude glycerol in sustainable polymers preparation, Int J Biol Macromol, 261 (2024) 129536.
[2] Y. Wang, Y. Xiao, G. Xiao, Sustainable value-added C_3 chemicals from glycerol transformations: A mini review for heterogeneous catalytic processes, Chinese Journal of Chemical Engineering, 27 (2019) 1536-1542.
[3] H. Xie, H. Wei, Z. Hu, S. Ge, Y. Guo, P. Guo, M. Wu, X. Jia, J. Li, T. Lu, Y. Zhang, W. Luo, Z. Wu, Enhanced production of lactic acid via glycerol selective oxidation over K-doped Pt/Sn-MFI catalysts, Chemical Engineering Journal, 511 (2025).
[4] A.L. Chun Minh, S.P. Samudrala, S. Bhattacharya, Valorisation of glycerol through catalytic hydrogenolysis routes for sustainable production of value-added C_3 chemicals: current and future trends, Sustainable Energy & Fuels, 6 (2022) 596-639.
[5] M.H. Mohamad, R. Awang, W.M. Yunus, A review of acetol: application and production, American Journal of Applied Sciences, 8 (2011) 1135.
[6] R.S. Disselkamp, B.D. Harris, T.R. Hart, Hydroxy acetone and lactic acid synthesis from aqueous propylene glycol/hydrogen peroxide catalysis on Pd-black, Catalysis Communications, 9 (2008) 2250-2252.
[7] P. Soucaille, I.M. Salles, F. Voelker, R. Figge, Microorganisms and methods for production of 1,2-propanediol and acetol, Google Patents, 2015.
[8] P. Soucaille, F. Voelker, R. Figge, Metabolically engineered microorganism useful for the production of 1, 2-propanediol, Google Patents, 2010.
[9] S. Basu, A.K. Sen, A Review on Catalytic Dehydration of Glycerol to Acetol, ChemBioEng Reviews, 8 (2021) 633-653.
[10] A. Abdullah, A. Zuhairi Abdullah, M. Ahmed, J. Khan, M. Shahadat, K. Umar, M.A. Alim, A review on recent developments and progress in sustainable acrolein production through catalytic dehydration of bio-renewable glycerol, Journal of Cleaner Production, 341 (2022) 130876.
[11] B.C.M. Morales, B.A.O. Quesada, Conversion of glycerol to hydroxyacetone over Cu and Ni catalysts, Catalysis Today, (2020).
[12] H. Zhao, L. Zheng, X. Li, P. Chen, Z. Hou, Hydrogenolysis of glycerol to 1,2-propanediol over Cu-based catalysts: A short review, Catalysis Today, 355 (2020) 84-95.
[13] J. Mazarío, P. Concepción, M. Ventura, M.E. Domine, Continuous catalytic process for the selective dehydration of glycerol over Cu-based mixed oxide, J. Catal., 385 (2020) 160-175.
[14] S. Sato, M. Akiyama, R. Takahashi, T. Hara, K. Inui, M. Yokota, Vapor-phase reaction of polyols over copper catalysts, Applied Catalysis A: General, 347 (2008) 186-191.
[15] R.B. Mane, A. Yamaguchi, A. Malawadkar, M. Shirai, C.V. Rode, Active sites in modified copper catalysts for selective liquid phase dehydration of aqueous glycerol to acetol, RSC Advances, 3 (2013).

[16] T. Gabrysch, B. Peng, S. Bunea, G. Dyker, M. Muhler, The Role of Metallic Copper in the Selective Hydrodeoxygenation of Glycerol to 1,2-Propanediol over Cu/ZrO_2, ChemCatChem, 10 (2018) 1344-1350.
[17] F. Fernandes Barbosa, T. Pinheiro Braga, Catalytic Conversion of Glycerol to Acetol and Acrolein Using Metal Oxides: Surface Reactions, Prospects and Challenges, ChemCatChem, 15 (2022).
[18] R.-P. Ye, L. Lin, Q. Li, Z. Zhou, T. Wang, C.K. Russell, H. Adidharma, Z. Xu, Y.-G. Yao, M. Fan, Recent progress in improving the stability of copper-based catalysts for hydrogenation of carbon–oxygen bonds, Catalysis Science & Technology, 8 (2018) 3428-3449.
[19] L. Zhang, P. Ai, Z. Gao, W. Huang, Enhanced catalytic stability of Cu-based catalyst for dimethyl oxalate hydrogenation, Fuel, 324 (2022).
[20] J. Mazarío, J.A. Cecilia, E. Rodríguez-Castellón, M.E. Domine, Highly dispersed copper oxide on silica: Towards an efficient catalyst for continuous glycerol dehydration to acetol, Applied Catalysis A: General, 652 (2023).
[21] E.S. Vasiliadou, A.A. Lemonidou, Kinetic study of liquid-phase glycerol hydrogenolysis over Cu/SiO_2 catalyst, Chemical Engineering Journal, 231 (2013) 103-112.
[22] T. Gabrysch, M. Muhler, B. Peng, The kinetics of glycerol hydrodeoxygenation to 1,2-propanediol over Cu/ZrO_2 in the aqueous phase, Applied Catalysis A: General, 576 (2019) 47-53.
[23] G.-S. He, L.-B. Sun, X.-L. Song, X.-Q. Liu, Y. Yin, Y.-C. Wang, Adjusting Host Properties to Promote Cuprous Chloride Dispersion and Adsorptive Desulfurization Sites Formation on SBA-15, Energy Fuels, 25 (2011) 3506-3513.
[24] D. Sun, Y. Yamada, S. Sato, Effect of Ag loading on Cu/Al_2O_3 catalyst in the production of 1,2-propanediol from glycerol, Applied Catalysis A: General, 475 (2014) 63-68.
[25] C.-J. Yue, M.-M. Gan, L.-P. Gu, Y.-F. Zhuang, In situ synthesized nano-copper over ZSM-5 for the catalytic dehydration of glycerol under mild conditions, Journal of the Taiwan Institute of Chemical Engineers, 45 (2014) 1443-1448.
[26] S. Sato, D. Sakai, F. Sato, Y. Yamada, Vapor-phase Dehydration of Glycerol into Hydroxyacetone over Silver Catalyst, Chemistry Letters, 41 (2012) 965-966.
[27] X. Dong, X. Ma, H. Xu, Q. Ge, Comparative study of silica-supported copper catalysts prepared by different methods: formation and transition of copper phyllosilicate, Catalysis Science & Technology, 6 (2016) 4151-4158.
[28] T. Ding, H. Tian, J. Liu, W. Wu, J. Yu, Highly active Cu/SiO_2 catalysts for hydrogenation of diethyl malonate to 1,3-propanediol, Chinese Journal of Catalysis, 37 (2016) 484-493.
[29] L. Chen, P. Guo, M. Qiao, S. Yan, H. Li, W. Shen, H. Xu, K. Fan, Cu/SiO_2 catalysts prepared by the ammonia-evaporation method: Texture, structure, and catalytic performance in hydrogenation of dimethyl oxalate to ethylene glycol, J. Catal., 257 (2008) 172-180.
[30] E. Yuan, P. Ni, W. Zhuang, R. Jian, P. Jian, Synergic catalysis by a CuO-like phase and Cu^0 for anaerobic dehydrogenation of 2,3-butanediol, J. Catal., 382 (2020) 256-268.
[31] F. Li, L. Wang, X. Han, P. He, Y. Cao, H. Li, Influence of support on the performance of copper catalysts for the effective hydrogenation of ethylene carbonate to synthesize ethylene glycol and methanol, RSC Advances, 6 (2016) 45894-45906.
[32] J.A.S. Costa, R.A. de Jesus, D.O. Santos, J.B. Neris, R.T. Figueiredo, C.M. Paranhos, Synthesis, functionalization, and environmental application of silica-based mesoporous materials of the M41S and SBA-n families: A review, Journal of Environmental Chemical Engineering, 9 (2021) 105259-105288.
[33] P. Verma, Y. Kuwahara, K. Mori, R. Raja, H. Yamashita, Functionalized mesoporous SBA-15 silica: recent trends and catalytic applications, Nanoscale, 12 (2020) 11333-11363.
[34] S. Singh, R. Kumar, H.D. Setiabudi, S. Nanda, D.-V.N. Vo, Advanced synthesis strategies of mesoporous SBA-15 supported catalysts for catalytic reforming applications: A state-of-the-art review, Applied Catalysis A: General, 559 (2018) 57-74.
[35] J. Shen, C. Hess, Controlling the dispersion of ceria using nanoconfinement: application to CeO_2/SBA-15 catalysts for NH_3-SCR, Materials Advances, 2 (2021) 7400-7412.

[36] A. Talebian-Kiakalaieh, N.A.S. Amin, H. Hezaveh, Glycerol for renewable acrolein production by catalytic dehydration, Renewable and Sustainable Energy Reviews, 40 (2014) 28-59.
[37] A. Lete, F. Lacleta, L. García, J. Ruiz, J. Arauzo, Effect of calcination temperature and atmosphere on the properties and performance of CuAl catalysts for glycerol dehydration to acetol, Biomass and Bioenergy, 195 (2025).
[38] B. Katryniok, S. Paul, V. Bellière-Baca, P. Rey, F. Dumeignil, Glycerol dehydration to acrolein in the context of new uses of glycerol, Green Chemistry, 12 (2010).
[39] J. Shan, Z. Li, Z. Chen, D. Wang, X. Zhang, Z. Ning, Y. Xue, S. Zhu, Enhancement in catalytic performance of HZSM-5 zeolite for glycerol dehydration after acidity regulation, Chemical Engineering Journal, 460 (2023).
[40] A. Bienholz, H. Hofmann, P. Claus, Selective hydrogenolysis of glycerol over copper catalysts both in liquid and vapour phase: Correlation between the copper surface area and the catalyst's activity, Applied Catalysis A: General, 391 (2011) 153-157.
[41] A.S. de Oliveira, S.J.S. Vasconcelos, J.R. de Sousa, F.F. de Sousa, J.M. Filho, A.C. Oliveira, Catalytic conversion of glycerol to acrolein over modified molecular sieves: Activity and deactivation studies, Chemical Engineering Journal, 168 (2011) 765-774.
[42] X.C. Jiang, C.H. Zhou, R. Tesser, M. Di Serio, D.S. Tong, J.R. Zhang, Coking of Catalysts in Catalytic Glycerol Dehydration to Acrolein, Industrial & Engineering Chemistry Research, 57 (2018) 10736-10753.
[43] M. Fedyna, M. Śliwa, K. Jaroszewska, L. Kępiński, J. Trawczyński, Procedure for the synthesis of AlSBA-15 with high aluminium content: Characterization and catalytic activity, Microporous and Mesoporous Materials, 292 (2020) 109701-109711.
[44] A. Vinu, V. Murugesan, W. Böhlmann, M. Hartmann, An Optimized Procedure for the Synthesis of AlSBA-15 with Large Pore Diameter and High Aluminum Content, The Journal of Physical Chemistry B, 108 (2004) 11496-11505.
[45] J.A. Cecilia, C. García-Sancho, J.M. Mérida-Robles, J. Santamaría-González, A. Infantes-Molina, R. Moreno-Tost, P. Maireles-Torres, Aluminum doped mesoporous silica SBA-15 for glycerol dehydration to value-added chemicals, Journal of Sol-Gel Science and Technology, 83 (2017) 342-354.
[46] Q. Li, Z. Wu, B. Tu, S.S. Park, C.-S. Ha, D. Zhao, Highly hydrothermal stability of ordered mesoporous aluminosilicates Al-SBA-15 with high Si/Al ratio, Microporous and Mesoporous Materials, 135 (2010) 95-104.
[47] M. Selvaraj, S. Kawi, D.-W. Park, C.-S. Ha, Synthesis and characterization of GaSBA-15: Effects of synthesis parameters and hydrothermal stability, Microporous and mesoporous materials, 117 (2009) 586-595.
[48] A. Vinu, D.P. Sawant, K. Ariga, K. Hossain, S. Halligudi, M. Hartmann, M. Nomura, Direct synthesis of well-ordered and unusually reactive FeSBA-15 mesoporous molecular sieves, Chemistry of materials, 17 (2005) 5339-5345.
[49] A. Carrero, A.J. Vizcaíno, J.A. Calles, L. García-Moreno, Hydrogen production through glycerol steam reforming using Co catalysts supported on SBA-15 doped with Zr, Ce and La, Journal of Energy Chemistry, 26 (2017) 42-48.
[50] S.-Y. Chen, C.-Y. Tang, J.-F. Lee, L.-Y. Jang, T. Tatsumi, S. Cheng, Effect of calcination on the structure and catalytic activities of titanium incorporated SBA-15, Journal of Materials Chemistry, 21 (2011) 2255-2265.
[51] Â. Silva, K. Wilson, A.F. Lee, V.C. dos Santos, A.C. Cons Bacilla, K.M. Mantovani, S. Nakagaki, Nb_2O_5/SBA-15 catalyzed propanoic acid esterification, Applied Catalysis B: Environmental, 205 (2017) 498-504.
[52] J.M. Rosenholm, T. Czuryszkiewicz, F. Kleitz, J.B. Rosenholm, M. Lindén, On the Nature of the Brønsted Acidic Groups on Native and Functionalized Mesoporous Siliceous SBA-15 as Studied by Benzylamine Adsorption from Solution, Langmuir, 23 (2007) 4315-4323.
[53] S. Xing, P. Lv, J. Fu, J. Wang, P. Fan, L. Yang, Z. Yuan, Direct synthesis and characterization of pore-broadened Al-SBA-15, Microporous and Mesoporous Materials, 239 (2017) 316-327.

[54] G. Muthu Kumaran, S. Garg, K. Soni, M. Kumar, J.K. Gupta, L.D. Sharma, K.S. Rama Rao, G. Murali Dhar, Synthesis and characterization of acidic properties of Al-SBA-15 materials with varying Si/Al ratios, Microporous and Mesoporous Materials, 114 (2008) 103-109.
[55] M.S.M.d. Oliveira, L. Bieseki, A.E.V.d. Alencar, T.P. Braga, S.B.C. Pergher, Incorporating Aluminum Into the Structure of SBA-15 by Adjusting the pH and Adding NaF, Materials Research, 22 (2019) 1-11.
[56] A. Ungureanu, B. Dragoi, V. Hulea, T. Cacciaguerra, D. Meloni, V. Solinas, E. Dumitriu, Effect of aluminium incorporation by the "pH-adjusting" method on the structural, acidic and catalytic properties of mesoporous SBA-15, Microporous and Mesoporous Materials, 163 (2012) 51-64.
[57] P. Bhange, D.S. Bhange, S. Pradhan, V. Ramaswamy, Direct synthesis of well-ordered mesoporous Al-SBA-15 and its correlation with the catalytic activity, Applied Catalysis A: General, 400 (2011) 176-184.
[58] S. Lin, L. Shi, M.M.L. Ribeiro Carrott, P.J.M. Carrott, J. Rocha, M.R. Li, X.D. Zou, Direct synthesis without addition of acid of Al-SBA-15 with controllable porosity and high hydrothermal stability, Microporous and Mesoporous Materials, 142 (2011) 526-534.
[59] J. Ma, L.-S. Qiang, J.-F. Wang, X.-B. Tang, D.-Y. Tang, Effect of different synthesis methods on the structural and catalytic performance of SBA-15 modified by aluminum, Journal of Porous Materials, 18 (2010) 607-614.
[60] S. Wu, Y. Han, Y.-C. Zou, J.-W. Song, L. Zhao, Y. Di, S.-Z. Liu, F.-S. Xiao, Synthesis of Heteroatom Substituted SBA-15 by the "pH-Adjusting" Method, Chemistry of Materials, 16 (2004) 486-492.
[61] J. Socci, A. Osatiashtiani, G. Kyriakou, T. Bridgwater, The catalytic cracking of sterically challenging plastic feedstocks over high acid density Al-SBA-15 catalysts, Applied Catalysis A: General, 570 (2019) 218-227.
[62] C. Li, Y. Wang, Y. Guo, X. Liu, Y. Guo, Z. Zhang, Y. Wang, G. Lu, Synthesis of Highly Ordered, Extremely Hydrothermal stable SBA-15/Al-SBA-15 under the Assistance of Sodium Chloride, Chemistry of Materials, 19 (2007) 173-178.
[63] M. Sari Yilmaz, S. Piskin, The removal of template from SBA-15 samples synthesized from different silica sources, Journal of Thermal Analysis and Calorimetry, 121 (2015) 1255-1262.
[64] Y. Duan, Y. Zhou, X. Sheng, Y. Zhang, S. Zhou, Z. Zhang, Influence of alumina binder content on catalytic properties of PtSnNa/AlSBA-15 catalysts, Microporous and Mesoporous Materials, 161 (2012) 33-39.
[65] Y. Ding, G. Yin, X. Liao, Z. Huang, X. Chen, Y. Yao, J. Li, A convenient route to synthesize SBA-15 rods with tunable pore length for lysozyme adsorption, Microporous and Mesoporous Materials, 170 (2013) 45-51.
[66] C. Pirez, J.-C. Morin, J.C. Manayil, A.F. Lee, K. Wilson, Sol-gel synthesis of SBA-15: Impact of HCl on surface chemistry, Microporous and Mesoporous Materials, 271 (2018) 196-202.
[67] T. Klimova, A. Esquivel, J. Reyes, M. Rubio, X. Bokhimi, J. Aracil, Factorial design for the evaluation of the influence of synthesis parameters upon the textural and structural properties of SBA-15 ordered materials, Microporous and Mesoporous Materials, 93 (2006) 331-343.
[68] J.d.O.N. Ribeiro, D.C.L. Vasconcelos, W.L. Vasconcelos, Importance of the Order of Addition of the Alumina Precursor and its Type Into Al-SBA-15 Mesoporous Materials for Use as Water Adsorbents, Materials Research, 22 (2018) 1-8.
[69] Q. Xin, A. Papavasiliou, N. Boukos, A. Glisenti, J.P.H. Li, Y. Yang, C.J. Philippopoulos, E. Poulakis, F.K. Katsaros, V. Meynen, P. Cool, Preparation of CuO/SBA-15 catalyst by the modified ammonia driven deposition precipitation method with a high thermal stability and an efficient automotive CO and hydrocarbons conversion, Applied Catalysis B: Environmental, 223 (2018) 103-115.
[70] G.S. Pawley, Unit-cell refinement from powder diffraction scans, Journal of Applied Crystallography, 14 (1981) 357-361.
[71] A. Bruker, Topas V2. 0, Profile and Structure Analysis Software for Powder Diffraction Data. User AMnula, Bruker AXS, Karlsruhe, Germany, (2000).

[72] A.A. Coelho, TOPASandTOPAS-Academic: an optimization program integrating computer algebra and crystallographic objects written in C++, Journal of Applied Crystallography, 51 (2018) 210-218.
[73] D. Balzar, Voigt-function model in diffraction line-broadening analysis, International union of crystallography monographs on crystallography, 10 (1999) 94-126.
[74] D. Balzar, Voigt-function model in diffraction line-broadening analysis, Defect and microstructure analysis by diffraction, (1999) 94-126.
[75] A.R. Stokes, A.J.C. Wilson, A method of calculating the integral breadths of Debye-Scherrer lines, Mathematical Proceedings of the Cambridge Philosophical Society, 38 (2008) 313-322.
[76] M. Tamura, K.-i. Shimizu, A. Satsuma, Comprehensive IR study on acid/base properties of metal oxides, Applied Catalysis A: General, 433-434 (2012) 135-145.
[77] S. Yurdakal, C. Garlisi, L. Özcan, M. Bellardita, G. Palmisano, Chapter 4 - (Photo)catalyst Characterization Techniques: Adsorption Isotherms and BET, SEM, FTIR, UV–Vis, Photoluminescence, and Electrochemical Characterizations, in: G. Marcì, L. Palmisano (Eds.) Heterogeneous Photocatalysis, Elsevier2019, pp. 87-152.
[78] D.G. Barton, M. Shtein, R.D. Wilson, S.L. Soled, E. Iglesia, Structure and Electronic Properties of Solid Acids Based on Tungsten Oxide Nanostructures, The Journal of Physical Chemistry B, 103 (1999) 630-640.
[79] H. Yu, X. Jia, P. Wang, Y. Xiong, W. Shan, C. Zhang, Z. Song, High efficiency Al modified mesoporous SBA-15 catalyst for biomass-derived γ-valerolactone decarboxylation to butene, Microporous and Mesoporous Materials, 327 (2021) 111432-111441.
[80] A. Ungureanu, A. Chirieac, C. Ciotonea, I. Mazilu, C. Catrinescu, S. Petit, E. Marceau, S. Royer, E. Dumitriu, Enhancement of the dispersion and catalytic performances of copper in the hydrogenation of cinnamaldehyde by incorporation of aluminium into mesoporous SBA-15 silica, Applied Catalysis A: General, 598 (2020) 117615-117623.
[81] R. Bardestani, G.S. Patience, S. Kaliaguine, Experimental methods in chemical engineering: specific surface area and pore size distribution measurements—BET, BJH, and DFT, The Canadian Journal of Chemical Engineering, 97 (2019) 2781-2791.
[82] J. Gajardo, J. Colmenares-Zerpa, A.F. Peixoto, D.S.A. Silva, J.A. Silva, F. Gispert-Guirado, J. Llorca, E.A. Urquieta-Gonzalez, J.B.O. Santos, J. Szanyi, C. Sepúlveda, M.G. Álvarez, R.J. Chimentão, Revealing the effects of high Al loading incorporation in the SBA-15 silica mesoporous material, Journal of Porous Materials, 30 (2023) 1687-1707.
[83] L.-F. Chen, P.-J. Guo, L.-J. Zhu, M.-H. Qiao, W. Shen, H.-L. Xu, K.-N. Fan, Preparation of Cu/SBA-15 catalysts by different methods for the hydrogenolysis of dimethyl maleate to 1,4-butanediol, Applied Catalysis A: General, 356 (2009) 129-136.
[84] H. Vargas-Villagrán, D. Ramírez-Suárez, G. Ramírez-Muñoz, L.A. Calzada, G. González-García, T.E. Klimova, Tuning of activity and selectivity of Ni/(Al)SBA-15 catalysts in naphthalene hydrogenation, Catalysis Today, 360 (2021) 27-37.
[85] A. Yin, X. Guo, W.-L. Dai, K. Fan, Effect of Si/Al Ratio of Mesoporous Support on the Structure Evolution and Catalytic Performance of the Cu/Al-HMS Catalyst, The Journal of Physical Chemistry C, 114 (2010) 8523-8532.
[86] M. Sadou, A. Saadi, M. Hadj Meliani, R.K. Suleiman, T.A. Saleh, Facile Preparation of Supported Copper-modified SBA-15 Catalysts for efficient Benzaldehyde Hydrogenation, Surfaces and Interfaces, 30 (2022).
[87] H. Zhang, C. Tang, Y. Lv, C. Sun, F. Gao, L. Dong, Y. Chen, Synthesis, characterization, and catalytic performance of copper-containing SBA-15 in the phenol hydroxylation, J Colloid Interface Sci, 380 (2012) 16-24.
[88] K.-k. Miao, X.-l. Luo, W. Wang, J.-l. Guo, S.-f. Guo, F.-j. Cao, Y.-q. Hu, P.-m. Chang, G.-d. Feng, One-step synthesis of Cu–SBA-15 under neutral condition and its oxidation catalytic performance, Microporous and Mesoporous Materials, 289 (2019).

[89] Q. Wang, Y. Chen, G. Yang, P. Deng, X. Lu, R. Ma, Y. Fu, W. Zhu, Low-Temperature Catalytic Hydrogenolysis of Guaiacol to Phenol over Al-Doped SBA-15 Supported Ni Catalysts, ChemCatChem, 12 (2020) 4930-4938.
[90] A. Chirieac, B. Dragoi, A. Ungureanu, C. Ciotonea, I. Mazilu, S. Royer, A.S. Mamede, E. Rombi, I. Ferino, E. Dumitriu, Facile synthesis of highly dispersed and thermally stable copper-based nanoparticles supported on SBA-15 occluded with P123 surfactant for catalytic applications, J. Catal., 339 (2016) 270-283.
[91] E. Yuan, C. Wu, G. Liu, G. Li, L. Wang, Effects of SBA-15 physicochemical properties on performance of Pd/SBA-15 catalysts in 2-ethyl-anthraquinone hydrogenation, Journal of Industrial and Engineering Chemistry, 66 (2018) 158-167.
[92] V. Boosa, V. Bilakanti, V.K. Velisoju, N. Gutta, S. Inkollu, V. Akula, An insight on the influence of surface Lewis acid sites for regioselective C H bond C_3-cyanation of indole using NH_4I and DMF as combined cyanide source over Cu/SBA-15 catalyst, Molecular Catalysis, 445 (2018) 43-51.
[93] R. Ouargli-Saker, N. Bouazizi, S. Lassouad, S. Ammar, J. Vieillard, F. Le Derf, A. Azzouz, Copper-loaded SBA-15 Silica with Improved Electron Mobility-Conductance and Capacitance Properties, Journal of Inorganic and Organometallic Polymers and Materials, 30 (2020) 5108-5117.
[94] G. Shanbhag, T. Joseph, S. Halligudi, Copper(II) ion exchanged AlSBA-15: A versatile catalyst for intermolecular hydroamination of terminal alkynes with aromatic amines, J. Catal., 250 (2007) 274-282.
[95] C.M. Chanquía, L. Andrini, J.D. Fernández, M.E. Crivello, F.G. Requejo, E.R. Herrero, G.A. Eimer, Speciation of Copper in Spherical Mesoporous Silicates: From the Microscale to Angstrom, The Journal of Physical Chemistry C, 114 (2010) 12221-12229.
[96] C.M. Chanquía, K. Sapag, E. Rodríguez-Castellón, E.R. Herrero, G.A. Eimer, Nature and Location of Copper Nanospecies in Mesoporous Molecular Sieves, The Journal of Physical Chemistry C, 114 (2010) 1481-1490.
[97] Y. Sun, F. Meng, Q. Ge, J. Sun, Importance of the Initial Oxidation State of Copper for the Catalytic Hydrogenation of Dimethyl Oxalate to Ethylene Glycol, ChemistryOpen, 7 (2018) 969-976.
[98] V. Subbaramaiah, V.C. Srivastava, I.D. Mall, Optimization of Reaction Parameters and Kinetic Modeling of Catalytic Wet Peroxidation of Picoline by Cu/SBA-15, Industrial & Engineering Chemistry Research, 52 (2013) 9021-9029.
[99] L. Yan, T. Fu, D. Zhao, J. Wang, N. Narkhede, H. Zheng, G. Zhang, Z. Li, Highly dispersed Cu supported on mesoporous Al-KIT-6 for oxidative carbonylation of methanol to dimethyl carbonate, Applied Organometallic Chemistry, 34 (2020).
[100] E.J.M. Hensen, D.G. Poduval, D.A.J.M. Ligthart, J.A.R. van Veen, M.S. Rigutto, Quantification of Strong Brønsted Acid Sites in Aluminosilicates, The Journal of Physical Chemistry C, 114 (2010) 8363-8374.
[101] E.J.M. Hensen, D.G. Poduval, V. Degirmenci, D.A.J.M. Ligthart, W. Chen, F. Maugé, M.S. Rigutto, J.A.R.v. Veen, Acidity Characterization of Amorphous Silica–Alumina, The Journal of Physical Chemistry C, 116 (2012) 21416-21429.
[102] J.M. Gallo, C. Bisio, G. Gatti, L. Marchese, H.O. Pastore, Physicochemical characterization and surface acid properties of mesoporous [Al]-SBA-15 obtained by direct synthesis, Langmuir, 26 (2010) 5791-5800.
[103] M. Liu, L. Grajciar, C.J. Heard, The role of defects in high-silica zeolite hydrolysis and framework healing, Microporous and Mesoporous Materials, 377 (2024).
[104] C.M. Chanquía, A.L. Cánepa, J. Bazán-Aguirre, K. Sapag, E. Rodríguez-Castellón, P. Reyes, E.R. Herrero, S.G. Casuscelli, G.A. Eimer, Copper-containing spherical mesoporous silicates prepared by template-ion exchange: A multitechnique characterization and oxidation properties, Microporous and Mesoporous Materials, 151 (2012) 2-12.
[105] F. Akti, S. Balci, T. Dogu, Effect of synthesis media pH and gel separation technique on properties of copper incorporated SBA-15 catalyst, Materials Chemistry and Physics, 236 (2019) 121776.

[106] A.T. Shah, B. Li, Z.E.A. Abdalla, Direct synthesis of Cu–SBA-16 by internal pH-modification method and its performance for adsorption of dibenzothiophene, Microporous and Mesoporous Materials, 130 (2010) 248-254.
[107] J.J. Bravo-Suárez, B. Subramaniam, R.V. Chaudhari, Ultraviolet–Visible Spectroscopy and Temperature-Programmed Techniques as Tools for Structural Characterization of Cu in CuMgAlOx Mixed Metal Oxides, The Journal of Physical Chemistry C, 116 (2012) 18207-18221.
[108] G. Koch, L. Schmack, T. Ressler, Tuning Size and Reducibility of Copper Oxide Particles Supported on SBA-15, ChemistrySelect, 1 (2016) 2040-2049.
[109] P.K. Sharma, M.A.L.R.M. Cortes, J.W.J. Hamilton, Y. Han, J.A. Byrne, M. Nolan, Surface modification of TiO_2 with copper clusters for band gap narrowing, Catalysis Today, 321-322 (2019) 9-17.
[110] M.P. Athira, R. Arun, S. Haridas, CuO impregnated SBA-15; an efficient catalyst for B–V oxidation of cyclohexanone to caprolactone, Journal of Porous Materials, (2023).
[111] I. Sobczak, J. Wisniewska, P. Decyk, M. Trejda, M. Ziolek, Activation of Ethanol Transformation on Copper-Containing SBA-15 and MnSBA-15 Catalysts by the Presence of Oxygen in the Reaction Mixture, Int J Mol Sci, 24 (2023).
[112] P.P. Upare, M.-G. Jeong, Y.K. Hwang, D.H. Kim, Y.D. Kim, D.W. Hwang, U.H. Lee, J.-S. Chang, Nickel-promoted copper–silica nanocomposite catalysts for hydrogenation of levulinic acid to lactones using formic acid as a hydrogen feeder, Applied Catalysis A: General, 491 (2015) 127-135.
[113] P. Gaudin, P. Fioux, S. Dorge, H. Nouali, M. Vierling, E. Fiani, M. Molière, J.-F. Brilhac, J. Patarin, Formation and role of Cu+ species on highly dispersed CuO/SBA-15 mesoporous materials for SO_x removal: An XPS study, Fuel Processing Technology, 153 (2016) 129-136.
[114] J. Zhang, Y. Wu, L. Li, X. Wang, Q. Zhang, T. Zhang, Y. Tan, Y. Han, Ti-SBA-15 supported Cu–MgO catalyst for synthesis of isobutyraldehyde from methanol and ethanol, RSC Advances, 6 (2016) 85940-85950.
[115] X. Chang, A.F. Liu, B. Cai, J.Y. Luo, H. Pan, Y.B. Huang, Catalytic Transfer Hydrogenation of Furfural to 2-Methylfuran and 2-Methyltetrahydrofuran over Bimetallic Copper-Palladium Catalysts, ChemSusChem, 9 (2016) 3330-3337.
[116] I. Beinik, M. Hellstrom, T.N. Jensen, P. Broqvist, J.V. Lauritsen, Enhanced wetting of Cu on ZnO by migration of subsurface oxygen vacancies, Nat Commun, 6 (2015) 8845.
[117] M.C. Biesinger, Advanced analysis of copper X-ray photoelectron spectra, Surface and Interface Analysis, 49 (2017) 1325-1334.
[118] D. Vargas-Hernández, J.M. Rubio-Caballero, J. Santamaría-González, R. Moreno-Tost, J.M. Mérida-Robles, M.A. Pérez-Cruz, A. Jiménez-López, R. Hernández-Huesca, P. Maireles-Torres, Furfuryl alcohol from furfural hydrogenation over copper supported on SBA-15 silica catalysts, Journal of Molecular Catalysis A: Chemical, 383-384 (2014) 106-113.
[119] L. Li, C. Hu, L. Zhang, B. Shi, More octahedral Cu(+) and surface acid sites in uniformly porous Cu-Al_2O_3 for enhanced Fenton catalytic performances, J Hazard Mater, 406 (2021) 124739.
[120] C.M.A. Parlett, L.J. Durndell, A. Machado, G. Cibin, D.W. Bruce, N.S. Hondow, K. Wilson, A.F. Lee, Alumina-grafted SBA-15 as a high performance support for Pd-catalysed cinnamyl alcohol selective oxidation, Catalysis Today, 229 (2014) 46-55.
[121] M. Haouas, F. Taulelle, C. Martineau, Recent advances in application of (27)Al NMR spectroscopy to materials science, Prog Nucl Magn Reson Spectrosc, 94-95 (2016) 11-36.
[122] L. Fu, X. Li, M. Liu, H. Yang, Insights into the nature of Cu doping in amorphous mesoporous alumina, Journal of Materials Chemistry A, 1 (2013).
[123] H. Mitta, P.K. Seelam, S. Ojala, R.L. Keiski, P. Balla, Tuning Y-zeolite based catalyst with copper for enhanced activity and selectivity in vapor phase hydrogenolysis of glycerol to 1,2-propanediol, Applied Catalysis A: General, 550 (2018) 308-319.
[124] V.L. Yfanti, E.S. Vasiliadou, A.A. Lemonidou, Glycerol hydro-deoxygenation aided by in situ H_2 generation via methanol aqueous phase reforming over a Cu–ZnO–Al_2O_3 catalyst, Catalysis Science & Technology, 6 (2016) 5415-5426.

[125] V.L. Yfanti, D. Ipsakis, A.A. Lemonidou, Kinetic study of liquid phase glycerol hydrodeoxygenation under inert conditions over a Cu-based catalyst, Reaction Chemistry & Engineering, 3 (2018) 559-571.
[126] Z. Huang, F. Cui, H. Kang, J. Chen, C. Xia, Characterization and catalytic properties of the CuO/SiO_2 catalysts prepared by precipitation-gel method in the hydrogenolysis of glycerol to 1,2-propanediol: Effect of residual sodium, Applied Catalysis A: General, 366 (2009) 288-298.
[127] D. Gallego-García, U. Iriarte-Velasco, M.A. Gutiérrez-Ortiz, J.L. Ayastuy, One-pot synthesized niobium-doped nickel catalysts for efficient hydrogen-free glycerol hydrogenolysis, Chemical Engineering Journal, 508 (2025).
[128] I. Sádaba, M. López Granados, A. Riisager, E. Taarning, Deactivation of solid catalysts in liquid media: the case of leaching of active sites in biomass conversion reactions, Green Chemistry, 17 (2015) 4133-4145.
[129] P. Lauriol-Garbey, G. Postole, S. Loridant, A. Auroux, V. Belliere-Baca, P. Rey, J.M.M. Millet, Acid–base properties of niobium-zirconium mixed oxide catalysts for glycerol dehydration by calorimetric and catalytic investigation, Applied Catalysis B: Environmental, (2011).